

Flavour tagged time dependent angular analysis of $B_s^0 \rightarrow J/\psi \phi$ decays with $J/\psi \rightarrow e^+e^-$

V. Batozskaya¹, K. Klimaszewski¹

¹*National Centre for Nuclear Research, Warsaw, Poland*

Abstract

This note provides a description of the analysis of $B_s^0 \rightarrow J/\psi \phi$ decays with e^+e^- final state for J/ψ meson decays. We reconstructed $11\,645 \pm 114$ signal events in the 2011 and 2012 data, corresponding to 3 fb^{-1} of data. We report a measurements of the CP -violating phase, ϕ_s , the width difference between light and heavy mass eigenstates, $\Delta\Gamma_s$, and the average width, Γ_s , in the B_s^0 system. We also report measurements of the separate CP phases and direct CP violation parameters for each polarisation of the $J/\psi \phi$ final state.

Contents

1	Introduction	1
2	Phenomenology	2
3	Data samples, event reconstruction, selection and trigger	5
3.1	Data samples	5
3.2	MC samples	5
3.3	Event Selection	5
3.4	Trigger	5
3.5	Monte Carlo reweighting	7
3.5.1	Correction of the PID response	9
3.6	Boosted Decision Tree	10
3.7	Peaking background	11
4	Mass fit	15
4.1	Background components	18
4.1.1	Combinatorial background	18
4.1.2	Partially reconstructed background	18
5	Decay time resolution	21
6	Decay time acceptance	23
6.1	Track reconstruction efficiency	24
7	Angular acceptance	27
7.1	Normalization weights from full simulation	27
8	Angular resolution	31
9	Flavour tagging	34
9.1	OS calibration on $B^+ \rightarrow J/\psi(\mu^+\mu^-)K^+$ and $B^+ \rightarrow J/\psi(e^+e^-)K^+$ decays	37
10	Results of likelihood fit	40
11	Systematic uncertainties	43
11.1	$M(J/\psi(e^+e^-)\phi)$ mass model	43
11.2	Angular acceptance	43
11.3	Angular resolution	43
11.4	Decay time resolution	43
11.5	Trigger efficiency	43
11.6	Flavour tagging	43
11.7	Length and momentum scale	43
11.8	Contribution from Λ_b^0 decays	43

11.9 Fit bias	43
11.10 Further checks	44
12 Conclusion	45
13 To-do list	46
A Analysis code	47
B Data/MC comparison	48
C BDT training	52
C.1 Boosted Decision Tree	52
C.2 Peaking background	53
D Comparison of $B_s^0 \rightarrow J/\psi(\mu^+\mu^-)K^+K^-$ and $B_s^0 \rightarrow J/\psi(e^+e^-)\phi$ distributions	55
References	56

¹ 1 Introduction

² The interference between B_s^0 meson decay amplitudes to $J/\psi X$ CP eigenstates directly
³ or via mixing gives rise to a measurable CP -violating phase ϕ_s . In the Standard Model
⁴ (SM), for $b \rightarrow c\bar{c}s$ transitions and ignoring subleading penguin contributions, this phase
⁵ is predicted to be $-2\beta_s$, where $\beta_s = \arg[(V_{ts}V_{tb}^*)/(V_{cs}V_{cb}^*)]$ and V_{ij} are the elements of
⁶ CKM quark flavour mixing matrix [1, 2]. The indirect determination via global fits to
⁷ experimental data gives $2\beta_s = 0.0364 \pm 0.0016$ rad [3]. This precise indirect determination
⁸ within the SM makes the measurement of ϕ_s interesting since new physics (NP) processes
⁹ could modify the phase if new particles were to contribute to the $B_s^0 - \bar{B}_s^0$ box diagrams [4, 5].

¹⁰ The direct measurements of ϕ_s using $B_s^0 \rightarrow J/\psi\phi$ decays with $J/\psi \rightarrow \mu^+\mu^-$ were
¹¹ made by the LHCb [6], ATLAS [7] and CMS [8] experiments at the LHC and the CDF [9]
¹² and D0 [10] experiments at the *Tevatron*. The LHCb collaboration has reported the
¹³ world's best measurement of $\phi_s = -0.010 \pm 0.039$ rad [6] as a combined result from
¹⁴ $B_s^0 \rightarrow J/\psi K^+K^-$ and $B_s^0 \rightarrow J/\psi\pi^+\pi^-$ decays based on 3 fb^{-1} of integrated luminosity.
¹⁵ So far, all experimental results are in agreement with the SM predictions. The precision
¹⁶ of the results can be increased by including additional decay modes. Such results can be
¹⁷ combined with those from the $B_s^0 \rightarrow J/\psi K^+K^-$ and $B_s^0 \rightarrow J/\psi\pi^+\pi^-$ decays [11, 12].

¹⁸ This analysis presents the ϕ_s measurement using a tagged flavour time dependent
¹⁹ angular analysis of $B_s^0 \rightarrow J/\psi(e^+e^-)\phi(K^+K^-)$ channel with 3 fb^{-1} of integrated luminosity
²⁰ collected by LHCb detector in pp collisions at a centre-of-mass energy of 7 TeV in 2011
²¹ and 8 TeV in 2012 at the LHC. The $B_s^0 \rightarrow J/\psi(e^+e^-)\phi(K^+K^-)$ channel brings about
²² 10 % of the $\mu^+\mu^-$ mode statistics and is an important verification of the golden channel,
²³ $B_s^0 \rightarrow J/\psi(\mu^+\mu^-)K^+K^-$, as kinematics for both channels are identical but sources of
²⁴ systematic uncertainties are different. In addition, the measurements of the decay width
²⁵ difference of the light (L) and heavy (H) B_s^0 mass eigenstates, $\Delta\Gamma_s \equiv \Gamma_L - \Gamma_H$, and the
²⁶ average B_s^0 decay width, $\Gamma_s \equiv (\Gamma_L + \Gamma_H)/2$, are presented.

²⁷ This note is structured as follows. Sec. 2 describes the phenomenology of the $B_s^0 \rightarrow J/\psi\phi$
²⁸ decay, in particular introducing the polarization dependent notation. Sec. 3 describes
²⁹ the data and simulation samples which are used in the analysis, including trigger and
³⁰ offline selections. The two types of Boosted Decision Trees are used in the selection and
³¹ they are described in Sec. 3.6. The reweighting of Monte Carlo samples is discussed in
³² Sec. 3.5. The fit of the B_s^0 mass distribution is given in Sec. 4. Sec. 5 describes the
³³ procedure for extracting and calibrating the decay time resolution model. Sec. 6 describes
³⁴ the dependence of the efficiency as a function of decay time caused by the trigger and offline
³⁵ selections. The same techniques as described in Ref. [11] are used to determine decay time
³⁶ acceptance from data and simulation. The angular acceptance is derived from simulation,
³⁷ as described in Sec. 7. The effect of angular resolution is described in Sec. 8. The flavour
³⁸ tagging algorithms and their calibration are documented in Sec. 9. Sec. 10 describes the
³⁹ final results for the $B_s^0 \rightarrow J/\psi(e^+e^-)\phi$ analysis. The sources of systematic uncertainties are
⁴⁰ described and their size estimated in Sec. 11. Conclusions are given in Sec. 12. Additional
⁴¹ details of parameters for the fits, decay time resolution parameterisation, analysis code
⁴² and background systematics are described in the Appendices.

⁴³ If there is $B_s^0 \rightarrow J/\psi \phi$ decay it means that $J/\psi \rightarrow e^+e^-$, otherwise it is indicated.

⁴⁴ 2 Phenomenology

⁴⁵ The theoretical differential decay rate for an initial B_s^0 (Eq. 1) is described by a sum of
⁴⁶ ten terms, corresponding to the four polarization (0, \parallel , \perp , S) amplitudes of the K^+K^-
⁴⁷ system and their interference [13]. Each of these can be factorized into a time dependent
⁴⁸ and an angular dependent components

$$\frac{d^4\Gamma(B_s^0 \rightarrow J/\psi \phi)}{dt d\cos\theta_K d\cos\theta_\ell d\phi} \propto \sum_{k=1}^{10} h_k(t) f_k(\Omega). \quad (1)$$

⁴⁹ The time dependent functions $h_k(t)$ are given as:

$$h_k(t) = N_k e^{-\Gamma t} \left[a_k \cosh \frac{\Delta\Gamma_s t}{2} + b_k \sinh \frac{\Delta\Gamma_s t}{2} + c_k \cos(\Delta m_s t) + d_k \sin(\Delta m_s t) \right]. \quad (2)$$

⁵⁰ The Δm_s is the mass difference between the B_s^0 mass eigenstates, $\Delta m_s = M_H - M_L$. The
⁵¹ coefficients N_k and a_k, \dots, d_k can be expressed in terms of ϕ_s and four complex transversity
⁵² amplitudes A_f at $t = 0$. The label f takes the values $\{\perp, \parallel, 0\}$ for the three P-wave
⁵³ amplitudes and S for the one S-wave amplitude. In the fit we parameterize each $A_f(0)$
⁵⁴ by its magnitude squared $|A_f(0)|^2$ and its phase δ_f , and adopt the convention $\delta_0 = 0$,
⁵⁵ $|A_\perp|^2 + |A_0|^2 + |A_\parallel|^2 = 1$ and $f_S = |A_S|^2 / (|A_S|^2 + |A_\perp|^2 + |A_0|^2 + |A_\parallel|^2) = |A_S|^2 / (|A_S|^2 + 1)$.
⁵⁶ For a particle produced in a B_s^0 flavour eigenstate, B_s^0 and \bar{B}_s^0 , the coefficients in Eq. 2
⁵⁷ and the angular functions $f_k(\Omega)$ are given in Table 1 where

$$S = \frac{2|\lambda|}{1+|\lambda|^2} \sin(\phi_s), \quad D = \frac{2|\lambda|}{1+|\lambda|^2} \cos(\phi_s) \quad \text{and} \quad C = \frac{1-|\lambda|^2}{1+|\lambda|^2}.$$

⁵⁸ We allow for possible CP violation in mixing and in the decay amplitudes through the
⁵⁹ inclusion of the parameter λ , which is defined as $\lambda = \eta_f \frac{q}{p} \frac{\bar{A}_f}{A_f}$, where q and p are the complex
⁶⁰ coefficients connecting the mass and flavour eigenstates, $|B_{L,H}\rangle = p|B_s^0\rangle \pm q|\bar{B}_s^0\rangle$, \bar{A}_f is the
⁶¹ analog of A_f for \bar{B}_s^0 and η_f is the CP -eigenvalue of the final state. With these conventions,
⁶² $\phi_s = -\arg(\lambda)$.

⁶³ By performing an angular analysis of the decay products one can separate statistically
⁶⁴ the contributions from the different amplitudes. Such an analysis requires a measurement
⁶⁵ of the three decay product angles $\Omega = \{\theta, \varphi, \psi\}$ defined in Fig. 1. In the coordinate system
⁶⁶ of the J/ψ rest frame (where the ϕ and B_s^0 meson move in the x direction, the z axis is
⁶⁷ perpendicular to the decay plane of $\phi \rightarrow K^+K^-$, with $p_y(K^+) \geq 0$), the transversity polar
⁶⁸ and azimuthal angles (θ, φ) describe the direction of the e^+ . In the rest frame of the ϕ
⁶⁹ meson, the angle ψ is the angle between x axis and the K^+ momentum.

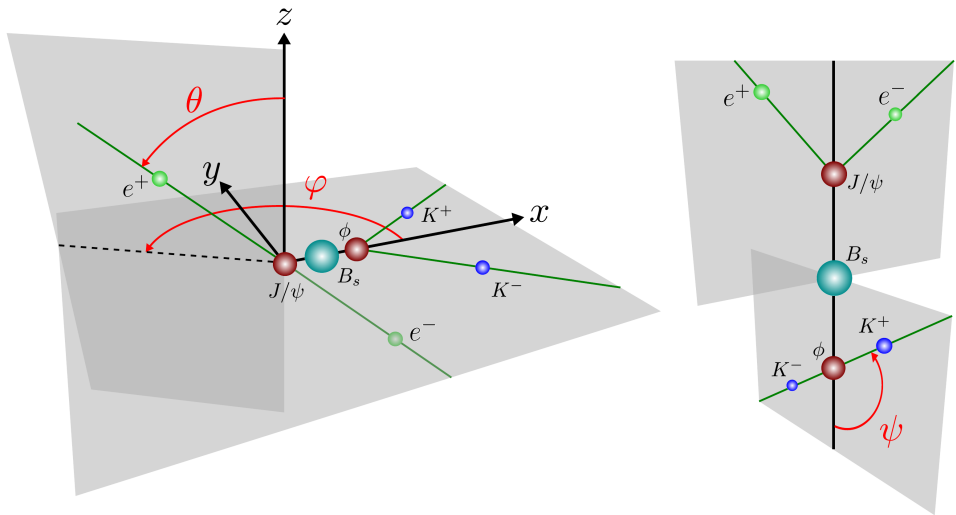


Figure 1: The angle definitions: θ is the angle formed by the positive lepton (e^+) and the z axis, in the J/ψ rest frame. The angle φ is the azimuthal angle of e^+ in the same frame. In the ϕ meson rest frame, ψ is the angle between $\vec{p}(K^+)$ and $-\vec{p}(J/\psi)$. The definitions are the same for both B_s^0 or a \bar{B}_s^0 decays.

Table 1: The angular and time dependent functions used in Equations 1 and 2.

k	$f_k(\theta_e, \theta_K, \phi_h)$	N_k	a_k	b_k	c_k	d_k
1	$2 \cos^2 \theta_K \sin^2 \theta_e$	$ A_0(0) ^2$	1	D	C	$-S$
2	$\sin^2 \theta_K (1 - \sin^2 \theta_e \cos^2 \phi_h)$	$ A_{\parallel}(0) ^2$	1	D	C	$-S$
3	$\sin^2 \theta_K (1 - \sin^2 \theta_e \sin^2 \phi_h)$	$ A_{\perp}(0) ^2$	1	$-D$	C	S
4	$\sin^2 \theta_K (1 - \sin^2 \theta_e \sin^2 \phi_h)$	$ A_{\parallel}(0)A_{\perp}(0) ^2$	$C \sin(\delta_{\perp} - \delta_{\parallel})$	$S \cos(\delta_{\perp} - \delta_{\parallel})$	$\sin(\delta_{\perp} - \delta_{\parallel})$	$\cos(\delta_{\perp} - \delta_{\parallel})$
5	$\frac{1}{2}\sqrt{2} \sin 2\theta_K \sin 2\theta_e \cos \phi_h$	$ A_0(0)A_{\parallel}(0) ^2$	$\cos(\delta_{\parallel} - \delta_0)$	$D \cos(\delta_{\parallel} - \delta_0)$	$C \cos(\delta_{\parallel} - \delta_0)$	$-S \cos(\delta_{\parallel} - \delta_0)$
6	$-\frac{1}{2}\sqrt{2} \sin 2\theta_K \sin 2\theta_e \sin \phi_h$	$ A_0(0)A_{\perp}(0) ^2$	$C \sin(\delta_{\perp} - \delta_0)$	$S \cos(\delta_{\perp} - \delta_0)$	$\sin(\delta_{\perp} - \delta_0)$	$D \cos(\delta_{\perp} - \delta_0)$
7	$\frac{2}{3} \sin^2 \theta_e$	$ A_S(0) ^2$	1	$-D$	C	S
8	$\frac{1}{3}\sqrt{6} \sin \theta_K \sin 2\theta_e \cos \phi_h$	$ A_S(0)A_{\parallel}(0) ^2$	$C \cos(\delta_{\parallel} - \delta_S)$	$S \sin(\delta_{\parallel} - \delta_S)$	$\cos(\delta_{\parallel} - \delta_S)$	$D \sin(\delta_{\parallel} - \delta_S)$
9	$-\frac{1}{3}\sqrt{6} \sin \theta_K \sin 2\theta_e \sin \phi_h$	$ A_S(0)A_{\perp}(0) ^2$	$\sin(\delta_{\perp} - \delta_S)$	$-D \sin(\delta_{\perp} - \delta_S)$	$C \sin(\delta_{\perp} - \delta_S)$	$S \sin(\delta_{\perp} - \delta_S)$
10	$\frac{4}{3}\sqrt{3} \cos \theta_K \sin^2 \theta_e$	$ A_S(0)A_0(0) ^2$	$C \cos(\delta_0 - \delta_S)$	$S \sin(\delta_0 - \delta_S)$	$\cos(\delta_0 - \delta_S)$	$D \sin(\delta_0 - \delta_S)$

70 **3 Data samples, event reconstruction, selection and**
71 **trigger**

72 **3.1 Data samples**

73 The candidates of $B_s^0 \rightarrow J/\psi(e^+e^-)\phi$ used in this analysis are selected from the data
74 sample taken in 2011 at $\sqrt{s} = 7$ TeV and 2012 at $\sqrt{s} = 8$ TeV. They are reconstructed
75 with version 14 of the reconstruction software (Reco14). The 2011 data are stripped
76 with version 21r1 (Stripping21r1-Merging-DV-v36r1), while the 2012 are stripped with
77 21 (Stripping21-Merging-DV-v36r1). In both cases, we use the Radiative stream and
78 the `StrippingBs2JpsieePhiDetachedLine`. The tuples are made on the GRID using
79 DA VINCI v37r2p4 with the track momentum scale calibration applied. Further processing
80 is performed offline¹ including application of the selection cuts, selection of single candidate
81 for events with multiple ones, as well as calculation of the sWeights, the procedure for which
82 is described in Sec. 4. The integrated luminosity is 0.9875 fb^{-1} in 2011 and 2.0399 fb^{-1}
83 in 2012.

84 **3.2 MC samples**

85 The Monte Carlo (MC) samples are produced with Sim08 and listed in Table 2. For each
86 event type, half of the sample is produced with PYTHIA6, half with PYTHIA8, each of
87 them being split equally into "magnet up" and "magnet down". The decays are preformed
88 with EVTGEN and PHOTOS++. The stripping is in "flagging mode", the reconstruction
89 is "Reco14a", no prescale and no spillover are applied. For 2011-like MC samples, the
90 trigger is simulated with MOORE v12r8g3 and TCK 0x40760037. For 2012 MC samples,
91 the trigger is simulated with MOORE v14r8p1 and TCK 0x409f0045. The main physics
92 parameters used in the simulation are summarized in Table 3. A track level smearing has
93 been applied to the simulated events to match the momentum resolution of the data.

94 **3.3 Event Selection**

95 For the events selected by the stripping line, first the $J/\psi \rightarrow e^+e^-$ decay is reconstructed,
96 then the $\phi \rightarrow K^+K^-$ decay and finally the $B_s^0 \rightarrow J/\psi\phi$ is looked for. Table 4 summarizes
97 the requirements in the stripping line as well as additional preselection requirements that
98 are applied.

99 **3.4 Trigger**

100 The stripping and final event selection are chosen in a way to not affect the decay time
101 acceptance. The trigger is the only source of the time dependent inefficiency is the trigger.
102 For this reason the trigger lines are divided into two categories: a decay time unbiased
103 and biased trigger lines. The trigger categories are defined as follows:

¹Details of the code can be found in Appendix A.

Table 2: Monte Carlo samples used in the analysis. All samples are produced with Sim08. The number of events quoted is the sum of PYTHIA6(MagUp)+PYTHIA6(MagDown)+PYTHIA8(MagUp)+PYTHIA8(MagDown), for 2011 plus 2012.

Decay Channel	Event type	Tot. number of events
Bs_Jpsiphi,ee=CPV,update2012,DecProdCut	13154001	20M
incl_Jpsi,ee=DecProdCut	24152001	20M
Bu_JpsiX,ee=JpsiInAcc	12952000	13.4M
Bd_JpsiX,ee=JpsiInAcc	11453001	11.6M
Bs_JpsiX,ee=JpsiInAcc	13454001	11M
Lb_JpsiX,ee=JpsiInAcc	15454101	11.4M
Lb_JpsipK,ee=phsp,DecProdCut	15154001	10M
Lb_Jpsippi,ee=phsp,DecProdCut	15154021	10M

Table 3: Decay model parameters for the Sim08 MC signal sample used in this analysis. The parameter values are based on those reported in Ref. [11].

Parameter	Value
Δm_s	17.8 ps^{-1}
$\Delta \Gamma_s$	0.0917 ps^{-1}
Γ_s	0.6653 ps^{-1}
ϕ_s	0.07 rad
$ A_0(0) ^2$	0.722
$ A_{\parallel}(0) ^2$	0.480
$ A_{\perp}(0) ^2$	0.499
$\delta_{\parallel} - \delta_0$	3.30 rad
$\delta_{\perp} - \delta_0$	3.07 rad

- 104 1. Unbiased: L0ElectronDecision_TOS or L0HadronDecision_TOS
- 105 2. Biased: (Hlt1TrackAllL0Decision_TOS and (Hlt2Topo(2,3,4)BodyBBDTDecision_TOS
106 or Hlt2TopoE(2,3,4)BodyBBDTDecision_TOS)) or Hlt2IncPhiDecision_TOS

107 The unbiased triggers correspond to approximately 72% and 81% of the selected events
108 in data and MC, respectively, as shown in Fig. 2.

109 The procedure to derive the decay time dependent efficiencies of these trigger categories
110 are described in Sec. 6.

Table 4: Selection criteria for $B_s^0 \rightarrow J/\psi \phi$ candidates in Stripping21r1 and preselection.

Decay mode	Cut parameter	Stripping	Preselection
$J/\psi \rightarrow e^+e^-$	$\Delta ln\mathcal{L}_{e\pi}$ $\chi_{\text{track}}^2/\text{ndf}(e)$ $\chi_{\text{IP}}^2(e)$ $p_{\text{T}}(e)$ $\chi_{\text{vtx}}^2/\text{ndf}(J/\psi)$ $p_{\text{T}}(J/\psi)$ $m(J/\psi)$	>0 <5 - $>500 \text{ MeV}/c$ <15 - $\in [2500, 3300] \text{ MeV}/c^2$	- <4 >0 - - $>400 \text{ MeV}/c$ -
$\phi \rightarrow K^+K^-$	$\Delta ln\mathcal{L}_{K\pi}$ $\chi_{\text{track}}^2/\text{ndf}(K)$ $p_{\text{T}}(K)$ $p(K)$ $\text{GhostProb}_{\text{track}}(K)$ $p_{\text{T}}(\phi)$ $\chi_{\text{vtx}}^2/\text{ndf}(\phi)$ $m(K^+K^-)$	- - - - - $>1000 \text{ MeV}/c$ <15 $\in [990, 1050] \text{ MeV}/c^2$	>0 <4 $>200 \text{ MeV}/c$ $>3000 \text{ MeV}/c$ <0.5 - <9 -
$B_s^0 \rightarrow J/\psi \phi$	$m(B_s^0)$ $\chi_{\text{vtx}}^2/\text{ndf}(B_s^0)$ $\chi_{\text{IP}}^2(B_s^0)$ t	$\in [4500, 6000] \text{ MeV}/c^2$ <10 - $>0.3 \text{ ps}$	$\in [4600, 6000] \text{ MeV}/c^2$ - <20 -

3.5 Monte Carlo reweighting

While there is in general a good agreement between data and MC for the samples used in this analysis, a significant difference exists in the event occupancy being largely underestimated in the simulated data. The occupancy correlates to the invariant mass shape of the signal as the correction of the electron momenta for the bremsstrahlung photons emitted before the magnet depends on proper measurement of particles energies in the electromagnetic calorimeter (ECAL). Therefore, it is important to properly include this effect in the MC. A way to accommodate data and MC difference is to use the scintillating pad detector (SPD) hits multiplicity distribution, which is highly correlated to the event occupancy. Therefore, a reweighting of the simulated events is applied in order to match their SPD multiplicity distribution to the LHCb data. The procedure used for this analysis is the same as described in Ref. [14].

The discrepancy in the SPD hit multiplicity between data and MC is presented in Fig. 3(a). The reweighting is performed separately for 2011 and 2012 as the average number of interactions per bunch crossing was different in the two years. The weights, which are applied to the simulation, are shown in Fig. 3(b). Comparison between data and MC before and after corrections are applied and they are shown in Appendix B.

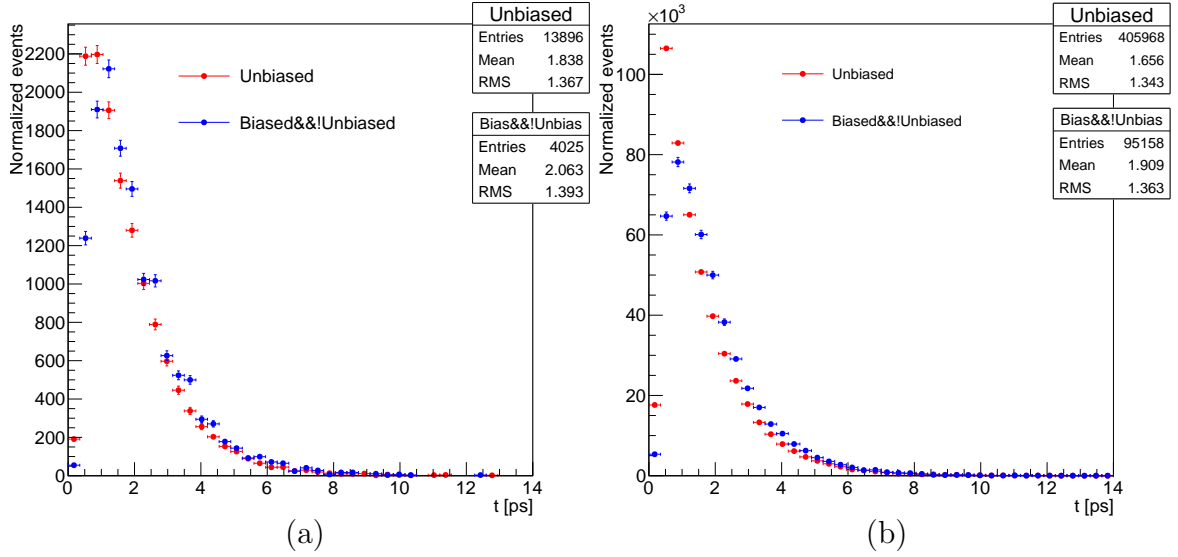


Figure 2: The decay time distribution of the events which are triggered by the unbiased triggers (red) and by the biased ones but not by unbiased (blue) for data (a) and MC (b).

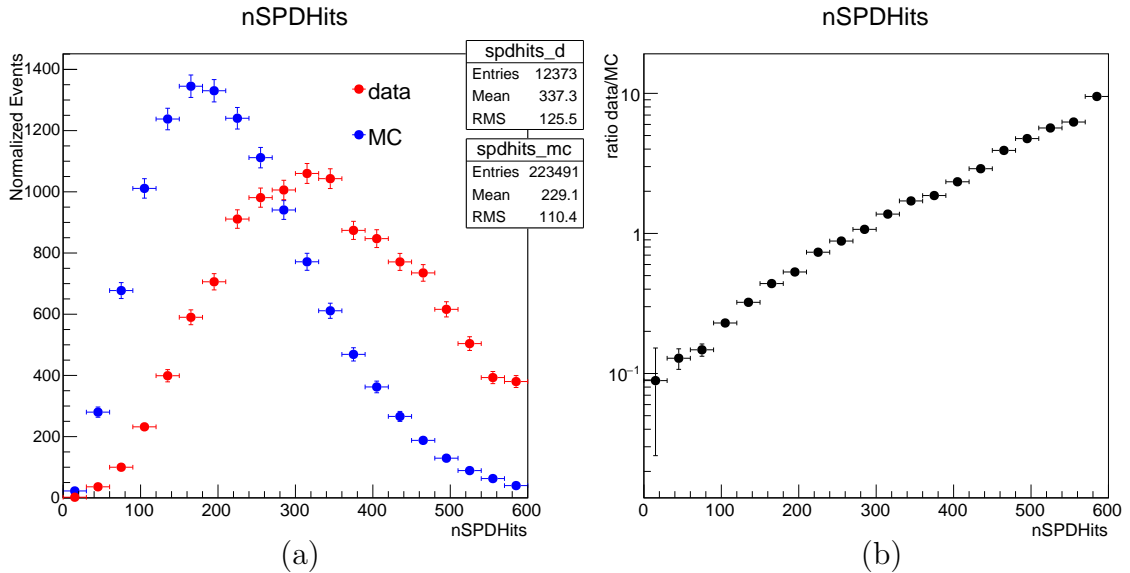


Figure 3: (a) The distribution of the number of hits in the SPD for $B_s^0 \rightarrow J/\psi(e^+e^-)\phi$ data and MC in 2012. (b) The ratio between data and MC distributions depends on the number of hits on the SPD. The ratio distribution is in logarithmic scale.

128 **3.5.1 Correction of the PID response**

129 The PID response is known to be not well simulated in the LHCb MC. Therefore, instead
 130 of applying the cut on the PID variables calculated in the MC, events are reweighted
 131 using PID efficiency tables. The **Urania/PIDCalib** package version **v4r0** is used to build
 132 PID efficiency tables for all final state particle types, K^\pm and e^\pm . The PID efficiencies are
 133 calculated in bins of η , p_T and number of tracks in the event. For each MC event the total
 PID efficiency is calculated and used to weight the event (Fig. 4).

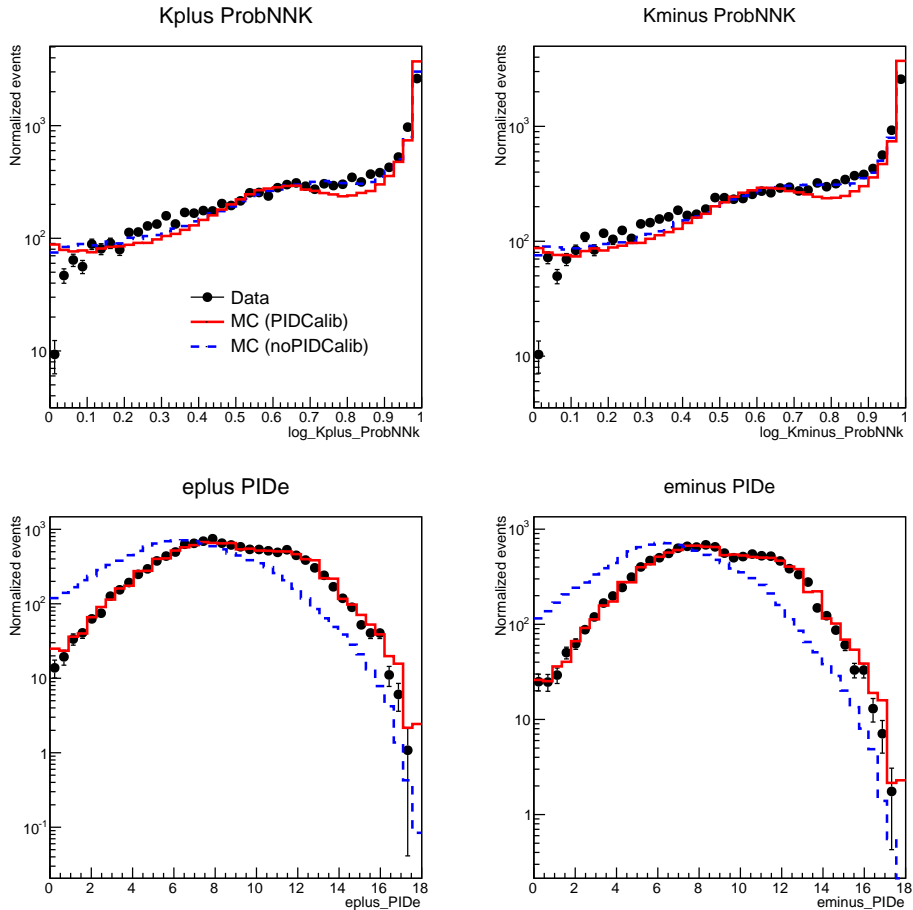


Figure 4: The ProbNNK(K^\pm) and PIDe(e^\pm) distributions for $B_s^0 \rightarrow J/\psi(e^+e^-)\phi$ in: data (black points), MC (blue dashed line) and **PIDCalib** simulated data (red solid line). All distributions are in logarithmic scale.

134 After applying **PIDCalib** algorithm the electron PIDe values for MC are in agreement
 135 with PID values for data. However, the opposite distributions obtained for ProbNN values
 136 of kaons. The kaon ProbNNK distributions for data are comparable with simulation without
 137 **PIDCalib**. Thus the corrected PIDe(e^\pm) and non-corrected ProbNNK(K^\pm) variables are
 138 used in the further selection (see Sec. 3.6).
 139

3.6 Boosted Decision Tree

After stripping and preselection criteria (Table 4), the amount of background events remaining in the sample is considerable and the additional selection is required. The Boosted Decision Tree (BDT) [15] are chosen to further discriminate the signal candidates from the background. In order to have a good agreement between data and simulation, a set of kinematic variables is chosen for the BDT discriminator. In particular 12 variables are taken into consideration:

- $p_T(J/\psi)$ - the transverse momentum of the J/ψ meson;
- $p_T(\phi)$ - the transverse momentum of the ϕ meson;
- $IP(B_s^0)$ - the impact parameter of the reconstructed B_s^0 meson with respect to the primary vertex;
- $\chi_{FD}^2(B_s^0)$ of the measured flight distance of the B_s^0 meson;
- χ_{IP}^2 of the impact parameter of the electron and positron;
- χ_{vtx}^2/ndf of the reconstructed secondary vertex;
- PIDe - the difference of log-likelihood between electron and pion hypothesis for the electron and positron. In case of MC the PIDe is reweighted using `PIDCalib` tool (Sec. 3.5.1) and is called PIDe_{corr};
- ProbNNK - Neural Net (NN) log-likelihood of the kaon hypothesis for the kaons;
- χ_{DTF}^2 of the reconstructed B_s^0 meson.

The training of the BDT is done using the following samples:

- Signal: the $B_s^0 \rightarrow J/\psi\phi$ simulated sample is used as signal model. This sample is required to pass exactly the same stripping and preselection criteria and, furthermore, the MC truth information is used to require that the reconstructed candidate matches with the generated decay.
- Background: a wrong sign $B_s^0 \rightarrow J/\psi\phi$ data sample is used. In particular $B_s^0 \rightarrow J/\psi(e^+e^-)\phi(K^+K^+)$, $B_s^0 \rightarrow J/\psi(e^+e^-)\phi(K^-K^-)$, $B_s^0 \rightarrow J/\psi(e^-e^-)\phi(K^+K^+)$, $B_s^0 \rightarrow J/\psi(e^-e^-)\phi(K^-K^-)$, $B_s^0 \rightarrow J/\psi(e^+e^+)\phi(K^+K^-)$, $B_s^0 \rightarrow J/\psi(e^-e^-)\phi(K^+K^-)$, $B_s^0 \rightarrow J/\psi(e^+e^-)\phi(K^+K^+)$ and $B_s^0 \rightarrow J/\psi(e^+e^-)\phi(K^-K^-)$ events make the background sample. Also these events are required to pass all the selection steps.

The choice to use a wrong sign $B_s^0 \rightarrow J/\psi\phi$ data sample instead of data events taken from the sidebands of the B_s^0 mass distribution is motivated by the fact that in this way the signal and background samples are more homogeneous. The sideband events from data ($M(B_s^0) < 5050$ MeV and $M(B_s^0) > 5550$ MeV) have also been considered to simulate the

174 background events in the BDT training. A worse agreement between sidebands data and
175 simulation is observed in the BDT performance description.

176 The ranking of variable importance used to train the BDT is shown in Table 5. The
177 BDT response is presented in Fig. 5a. The further details on the BDT, including plots
178 comparing the input variable distributions between signal and background, are presented
in Appendix C.

Table 5: The ranking of variable importance used in BDT selection.

Rank	Variable	Importance
1	$\log(\text{ProbNNK})(K^+)$	1.149e-01
2	$\text{PID}(e^-)_{\text{corr}}$	1.075e-01
3	$\log(\text{ProbNNK})(K^-)$	1.066e-01
4	$\log(\chi^2_{\text{IP}})(e^-)$	9.723e-02
5	$\text{PID}(e^+)_{\text{corr}}$	9.430e-02
6	$\log(\chi^2_{\text{IP}})(e^+)$	8.902e-02
7	$p_T(\phi)$	8.500e-02
8	$\text{IP}(B_s^0)$	8.456e-02
9	$\chi^2_{\text{vtx}}(B_s^0)$	7.939e-02
10	$p_T(J/\psi)$	7.595e-02
11	$\log(\chi^2_{\text{DTF}})(B_s^0)$	6.565e-02
12	$\chi^2_{\text{FD}}(B_s^0)$	0.000e+00

179
180 The BDT response is the combined vote of many individual decision trees. It can be
181 used as a univariate discriminant to distinguish signal from background. To choose where
182 to cut on the BDT response we use a figure of merit (FoM) value (Eq. 3) [16], which is
183 defined as an effective size of the signal defined using the signal sWeight w_i :

$$FoM = \frac{(\sum_{i=1}^N w_i)^2}{\sum_{i=1}^N w_i^2}. \quad (3)$$

184 The sWeight is calculated using the sPlot technique [17] of statistical separation of signal
185 events from background. The Fig. 5b presents the dependence of the B_s^0 FoM value on
186 the BDT response. The optimal cut which maximises the signal size of selected events
187 with BDT response is chosen larger than 0.4.

188 3.7 Peaking background

189 The possible source of a background that peaks under the signal B_s^0 mass distribution is
190 considered as the $\Lambda_b^0 \rightarrow J/\psi(e^+e^-)pK$ decay, where a proton may be misidentified as a kaon.
191 To estimate the expected background amount, the $\Lambda_b^0 \rightarrow J/\psi pK$ is reconstructed in the
192 similar scheme as the analyzed decay. The transverse momentum and mass distributions
193 of the simulated signal $B_s^0 \rightarrow J/\psi\phi$ and background $\Lambda_b^0 \rightarrow J/\psi pK$ channels are presented

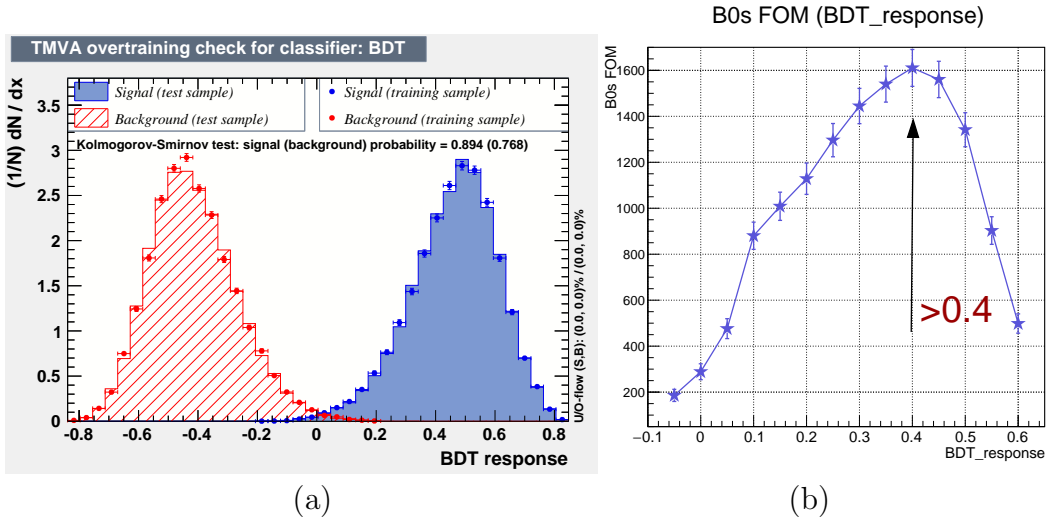


Figure 5: (a) The distributions of the BDT classifier for $B_s^0 \rightarrow J/\psi \phi$ training samples. The signal is red hatched filled while the background is blue solid filled. (b) The distribution of the FoM value vs. cut on the BDT response.

in Fig. 6. The number of simulated signal events is 557 908 with 6 323 $\Lambda_b^0 \rightarrow J/\psi pK$ events passing through the selection.

To reduce the contribution of $\Lambda_b^0 \rightarrow J/\psi pK$ decay, a second BDT is trained using the following samples:

- Signal: the simulated $B_s^0 \rightarrow J/\psi \phi$ sample is used as the signal model. This sample is required to pass exactly the same stripping and preselection criteria as described in Sec. 3.3. Furthermore the MC truth information is used to require that the reconstructed candidate matches with the generated decay.
- Background: the simulated $\Lambda_b^0 \rightarrow J/\psi pK$ sample reconstructed as a signal channel is used. Also these events are required to pass all the selection steps.

A set of 13 kinematic variables is taken as an input for the BDT discriminator, where 12 variables are the same as used in the first BDT training (Sec. 3.6). The additional variable is the log-likelihood of the proton hypothesis for a kaon and it is the variable with the largest importance for the BDT technique. The ranking of the variable importance used to train the BDT is shown in Table 6. The plots comparing the input variable distributions between signal and background are shown in Appendix C.

In the case of second BDT training, the BDT classifier distribution doesn't have a good separation of signal from background since the variables for trained samples have similar distributions and values (Fig. 7a). For these reasons, it is not possible to build a FoM based on sWeights. Therefore a new figure of merit (FoM2) is used to define a selection criterium:

$$FoM2 = \frac{S}{\sqrt{S + B1 + B2}}, \quad (4)$$

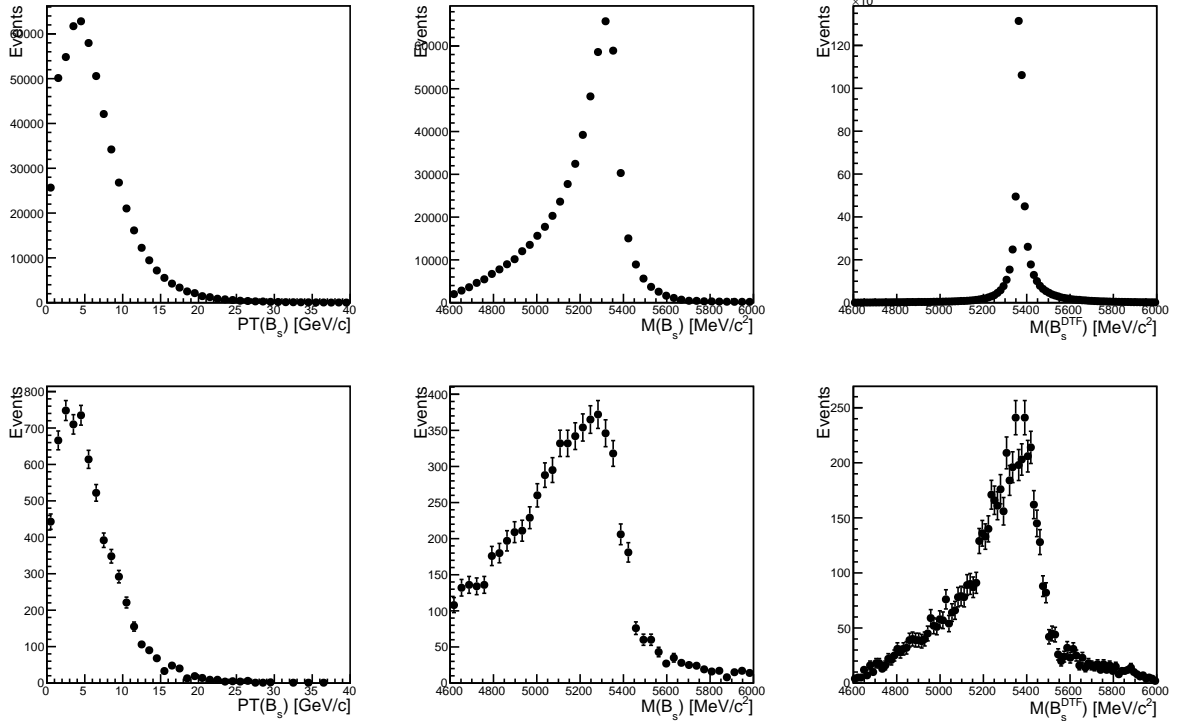


Figure 6: The transverse momentum and mass distributions of signal $B_s^0 \rightarrow J/\psi \phi$ events (top) and $\Lambda_b^0 \rightarrow J/\psi pK$ events reconstructed as $B_s^0 \rightarrow J/\psi \phi$ decay (bottom). The distributions correspond to 2012 simulated sample.

where S , $B1$ and $B2$ are the number of the signal and two types of the background events, respectively. The $B1$ and $B2$ background events are defined by the exponential and Gaussian functions, respectively. A two Crystal Ball functions with a common mean determine the signal shape. The mass fits are shown in Sec. 4. The dependence of the FOM2 value on BDT response cut is shown in Fig. 7b. All FOM values are consistent to each other within the limits of uncertainty. The optimal cut of >0.15 is chosen to select the final data sample.

After applying this cut the number of the $\Lambda_b^0 \rightarrow J/\psi pK$ events is in the MC sample has decreased by 44.5%. This corresponds to decrease the number of $B_s^0 \rightarrow J/\psi \phi$ candidates by 4.2% for the data sample.

Table 6: The ranking of the variable importance used in peaking background BDT selection.

Rank	Variable	Importance
1	$\log(\text{ProbNNp})(K^+)$	1.503e-01
2	$\log(\text{ProbNNK})(K^-)$	1.413e-01
3	$\chi_{\text{vtx}}^2(B_s^0)$	1.338e-01
4	$\log(\chi_{\text{IP}}^2)(e^+)$	1.316e-01
5	$\log(\chi_{\text{IP}}^2)(e^-)$	9.461e-02
6	$\log(\text{ProbNNK})(K^+)$	8.547e-02
7	$p_T(J/\psi)$	8.475e-02
8	$p_T(\phi)$	7.417e-02
9	$\text{PID}(e^-)_{\text{corr}}$	3.015e-02
10	$\text{IP}(B_s^0)$	2.547e-02
11	$\text{PID}(e^+)_{\text{corr}}$	2.455e-02
12	$\log(\chi_{\text{DTF}}^2)(B_s^0)$	2.387e-02
13	$\chi_{\text{FD}}^2(B_s^0)$	0.000e+00

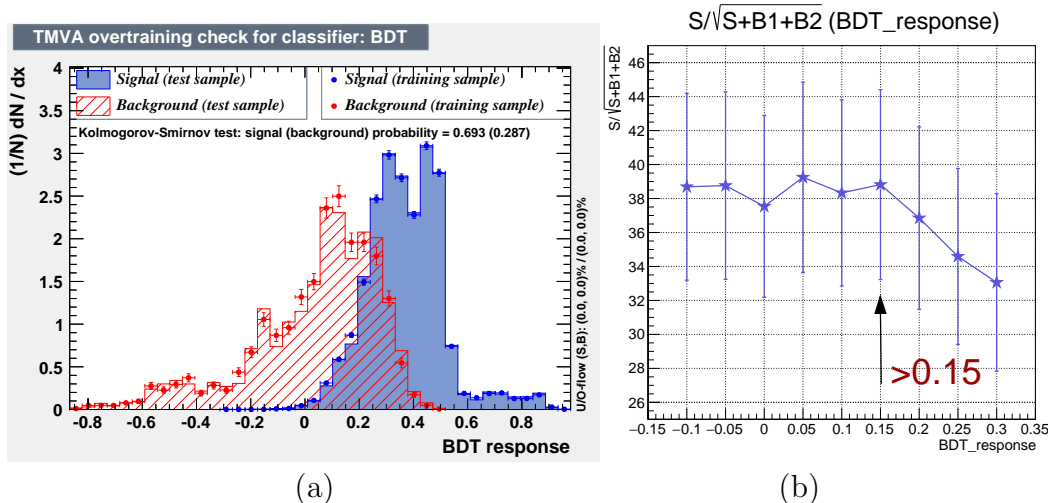


Figure 7: (a) The distributions of the peaking background BDT classifier for $B_s^0 \rightarrow J/\psi \phi$ training samples. The signal is red hatched filled while background is blue solid filled. (b) The distribution of the FoM2 value in depends on the BDT response cut.

225 4 Mass fit

226 The J/ψ and ϕ mass fit result after all selection steps (Sec. 3.3-3.7) using 3 fb^{-1} data
 227 sample is presented in Fig. 8. The J/ψ mass fit is performed using a sum of two Crystal
 228 Ball functions with a common mean for the signal and a polynomial function for the
 229 background events. In case of the ϕ meson, as a mass model a sum of double Gaussian
 230 and Voigtian functions [18] is used with a common mean for the signal candidates and a
 231 Chebychev polynomial for the background. The signal and the background yields from
 232 the fits to the two mesons are performed separately for 2011 and 2012 and the results are
 shown in Table 7.

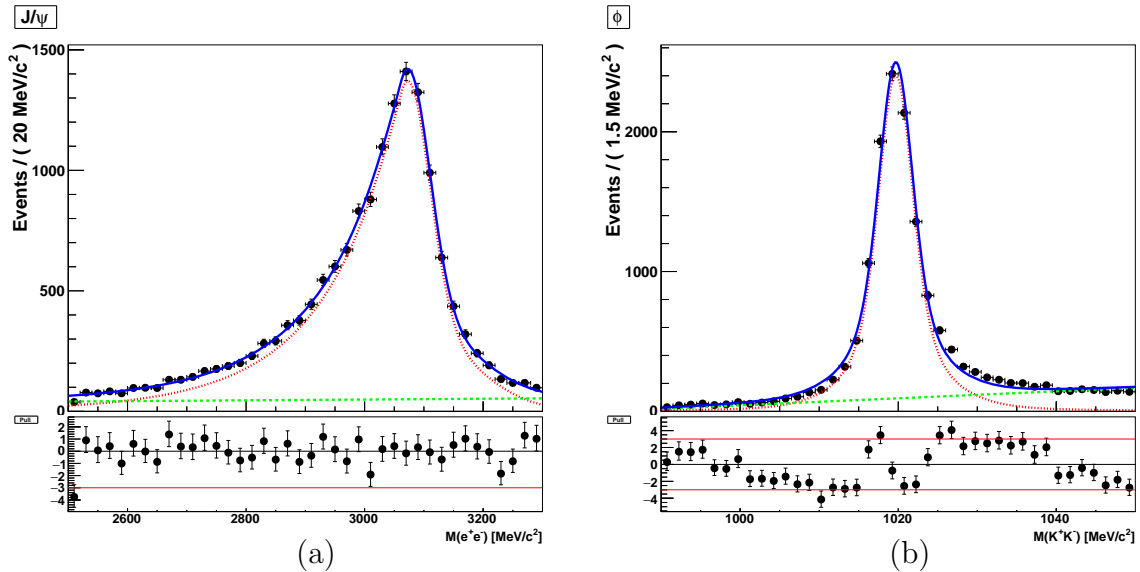


Figure 8: The invariant mass distributions of the (a) $J/\psi \rightarrow e^+e^-$ and (b) $\phi \rightarrow K^+K^-$ systems for the selected data sample of $B_s^0 \rightarrow J/\psi\phi$ candidates. The solid blue line shows the total fit, the signal and combinatorial background components are given by dotted red line and dashed green line, respectively.

Table 7: The signal and the background yields from fits to the J/ψ and ϕ mass distributions, separately in 2011 and 2012.

Year	2011	2012
J/ψ bkg	771 ± 57	$1\,525 \pm 88$
J/ψ signal	$3\,833 \pm 79$	$9\,551 \pm 126$
ϕ bkg	990 ± 48	$2\,632 \pm 69$
ϕ signal	$3\,613 \pm 70$	$8\,444 \pm 103$

233
 234 For the B_s^0 mass fit a signal model composed of a two Crystal Ball functions with a
 235 common mean is performed. The background model consists of an exponential function
 236 for the combinatorial component and a Gaussian function for the partially reconstructed
 237 events (Fig. 9a). The partially reconstructed background (Bkg2) consists mainly of excited
 238 charmonium resonances and will be described in Sec. 4.1.2. The fitted parameter values
 239 for the two 2011 and 2012 data samples are given in Table 8, along with the signal and
 240 two background yields.

241 The B_s^0 mass distribution with the mass of e^+e^- system constrained to the PDG mass
 242 of J/ψ [19], obtained using Decay Tree Fitter (DTF), is shown in Fig. 9b. The mass model
 243 is a sum of double Gaussian and Breit-Wigner functions with a common mean for the
 244 signal candidates. The model describing combinatorial background is an exponential, two
 245 Gaussian functions are used to describe the partially reconstructed background (Sec. 4.1.2).
 246 The fitted parameter values for the two 2011 and 2012 data samples are shown in Table 9,
 247 along with the signal and three background yields. The number of signal events is 11
 248 645 ± 114 for the full 2011 and 2012 data sample, which corresponds to 12% of the signal
 249 events from the $\mu^+\mu^-$ decay mode of $B_s^0 \rightarrow J/\psi\phi$.

250 The mass fit results for the B_s^0 without and with DTF are in agreement to each other.
 251 The B_s^0 mass distributions in a logarithmic scale are shown in Fig. 9.

Table 8: The results of the fit to the B_s^0 mass distribution, separately for 2011 and 2012 data samples. The signal shape is modeled by a sum of the two Crystal Ball functions with a common mean. The partially reconstructed background is modeled as a Gaussian function. The combinatorial background shape is an exponential.

Parameter	2011	2012
α_1^{CB}	1.90 ± 0.510	2.60 ± 1.20
α_2^{CB}	0.10 ± 0.062	0.15 ± 0.02
$\sigma_1 [\text{MeV}/c^2]$	100 ± 3.1	100 ± 0.45
$\sigma_2 [\text{MeV}/c^2]$	29 ± 3.3	33 ± 1.4
$\sigma_{Bkg2} [\text{MeV}/c^2]$	68 ± 26	74 ± 8.3
$\mu [\text{MeV}/c^2]$	$5\ 353 \pm 3.9$	$5\ 349 \pm 1.7$
$\mu_{Bkg2} [\text{MeV}/c^2]$	$4\ 739 \pm 20$	$4\ 734 \pm 8.8$
f	0.336 ± 0.070	0.304 ± 0.053
Bkg slope	-0.0034 ± 0.0004	-0.0031 ± 0.00002
N_{Bkg1}	689 ± 77	586 ± 76
N_{Bkg2}	258 ± 48	$1\ 163 \pm 123$
N_{Sig}	$3\ 656 \pm 73$	$9\ 327 \pm 119$

252 The fit performed to the reconstructed $J/\psi(e^+e^-)\phi$ mass distribution with DTF
 253 (Fig. 9b) is used to generate the event weights (sWeights) using the sPlot technique [17].
 254 The weights are used in the time dependent angular analysis. The fits to the J/ψ , ϕ and

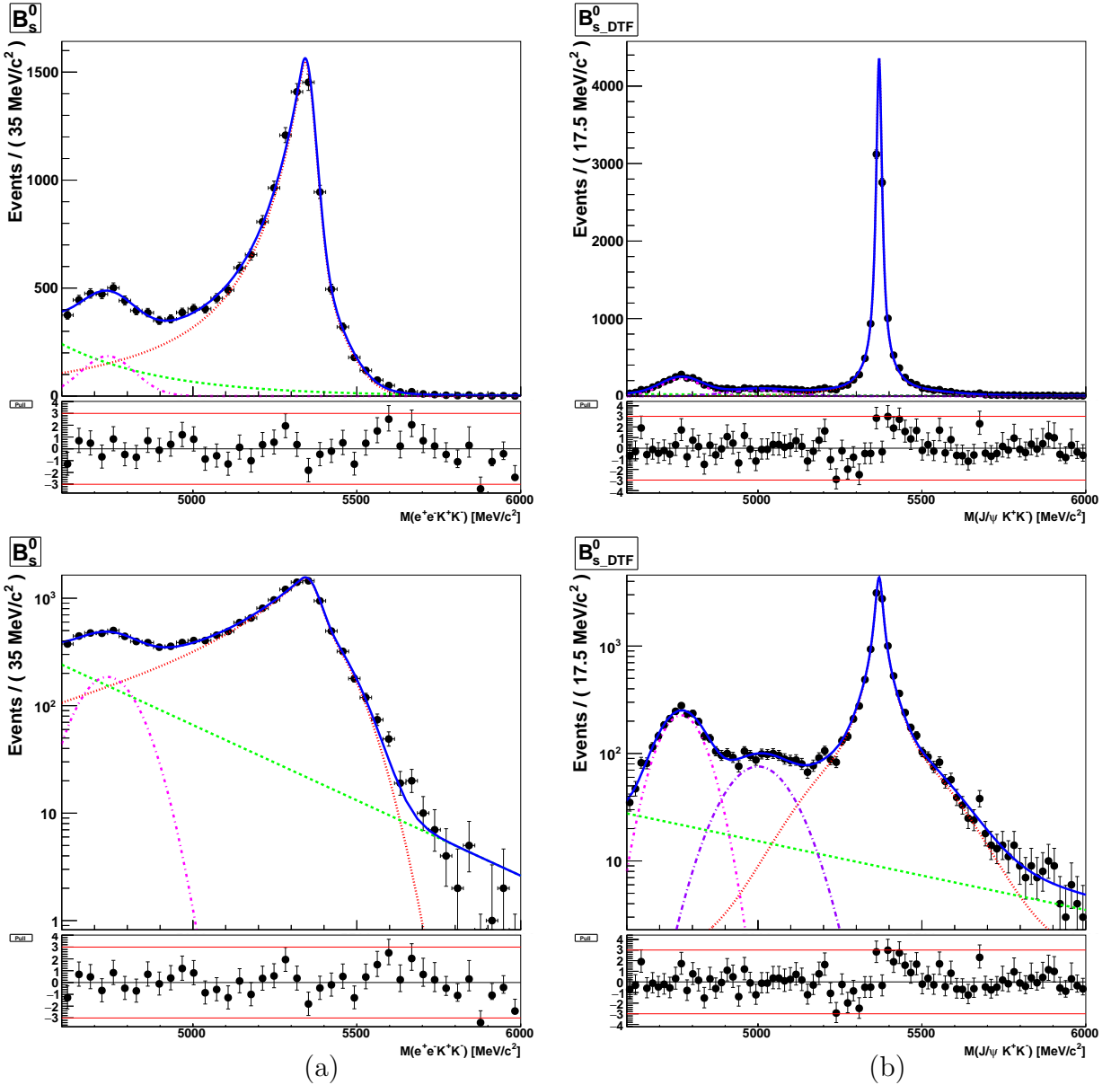


Figure 9: The invariant mass distributions of the (a) B_s^0 and (b) B_s^0 using DTF in the selected data sample of $B_s^0 \rightarrow J/\psi\phi$ candidates. The solid blue line shows the total fit, the signal and combinatorial background components are given by dashed red line and dotted green line, respectively. The partially reconstructed background contributions are given by dash-dotted pink and violet lines. The top and bottom plots are linear and logarithmic scale, respectively.

²⁵⁵ B_s^0 mass distributions are not subsequently used in the analysis and they simply help to
²⁵⁶ illustrate the data sample.

Table 9: The results of the fit to the B_s^0 mass distribution with DTF, separately for 2011 and 2012 data samples. The signal shape is a sum of double Gaussian and Breit-Wigner functions with a common mean. The two partially reconstructed backgrounds are modeled by two Gaussians. The combinatorial background shape is an exponential function.

Parameter	2011	2012
$\sigma_1[\text{MeV}/c^2]$	147 ± 23	158 ± 12
$\sigma_2[\text{MeV}/c^2]$	8.1 ± 0.92	45 ± 6.3
$\sigma_3[\text{MeV}/c^2]$	50 ± 11	23 ± 1.1
$\sigma_{bkg2}[\text{MeV}/c^2]$	60 ± 6.3	65 ± 4.4
$\sigma_{bkg3}[\text{MeV}/c^2]$	109 ± 20	90 ± 9.2
f_1	0.11 ± 0.035	0.17 ± 0.017
f_2	0.24 ± 0.065	0.12 ± 0.026
$\mu[\text{MeV}/c^2]$	5370 ± 0.36	5370 ± 0.23
$\mu_{bkg2}[\text{MeV}/c^2]$	4757 ± 5.2	4770 ± 3.4
$\mu_{bkg3}[\text{MeV}/c^2]$	4978 ± 25	5006 ± 9.8
bkg slope	-0.0015 ± 0.0005	-0.0018 ± 0.0004
N_{bkg}	340 ± 57	544 ± 78
N_{bkg2}	587 ± 33	$1\,470 \pm 52$
N_{bkg3}	307 ± 31	727 ± 41
N_{sig}	$3\,369 \pm 62$	$8\,336 \pm 96$

257 4.1 Background components

258 4.1.1 Combinatorial background

259 The random combinatorial background arises when not all of the four tracks originate
260 from the B_s^0 meson. This is modeled by an exponential function, the slope of which is left
261 floating in the fit cases.

262 4.1.2 Partially reconstructed background

263 The partially reconstructed background arises from the true B_s^0 decays but with one or
264 more tracks missing in the reconstruction. In the case of $B_s^0 \rightarrow J/\psi(e^+e^-)\phi$, there are two
265 sources for these partially reconstructed events: those are from the hadronic part, such as
266 events with $\phi(1020)$ resonance, called partially reconstructed hadronic background in the
267 following, and those are from the J/ψ part, called partially reconstructed J/ψ background
268 in the following, such as events from $\psi(2S)$ and $\chi_{c1}(1P)$ decays. In order to study the
269 background, a dedicated inclusive $B_s^0 \rightarrow J/\psi(e^+e^-)X$ MC sample is used. The sample
270 consists of 8 million events and is required to pass all selection cuts, as well as a veto on
271 true $B_s^0 \rightarrow J/\psi(e^+e^-)\phi$ events. The surviving events are split into four categories:

- 272 • both the J/ψ and the ϕ mesons are decay products of the B_s^0 meson;

- 273 • the J/ψ meson originates from excited charmonium resonances;
 274 • the ϕ meson is a product of one of the hadronic resonances;
 275 • neither J/ψ nor ϕ are decay products of the B_s^0 meson.

276 The B_s^0 mass distribution with the reconstructed J/ψ mass and constraint J/ψ mass for
 277 all categories are shown in Fig. 10 and 11. Most of the events are from the J/ψ part (black
 278 points in Fig. 10) where 46.9% is from $\psi(2S)$ decaying into J/ψ and 35.4% originates from
 279 $\chi_{c1}(1P)$ decays. The remaining part of the events comes from $\chi_{c0}(1P)$ (0.4%), $\chi_{c2}(1P)$
 280 (1.7%) and $h_c(1P)$ (0.6%) decays as shown in Fig. 11. The 15% of the events account for
 281 the "none" type (default code 0 for a particle [20]) that mean pure phase space decays,
 282 according to the given branching ratios. Only 4% of partially reconstructed background is
 283 due to the hadronic part (blue points in Fig. 10) which is η' , B_s^{0*} and $b\bar{b}$ decays.

284 The $B_s^0 \rightarrow J/\psi(e^+e^-)X$ simulated sample is only used to distinguish the different type
 285 of partially reconstructed background in B_s^0 mass distributions in the data sample. The
 286 mass fit is not applied to partially reconstructed background in the simulated sample.

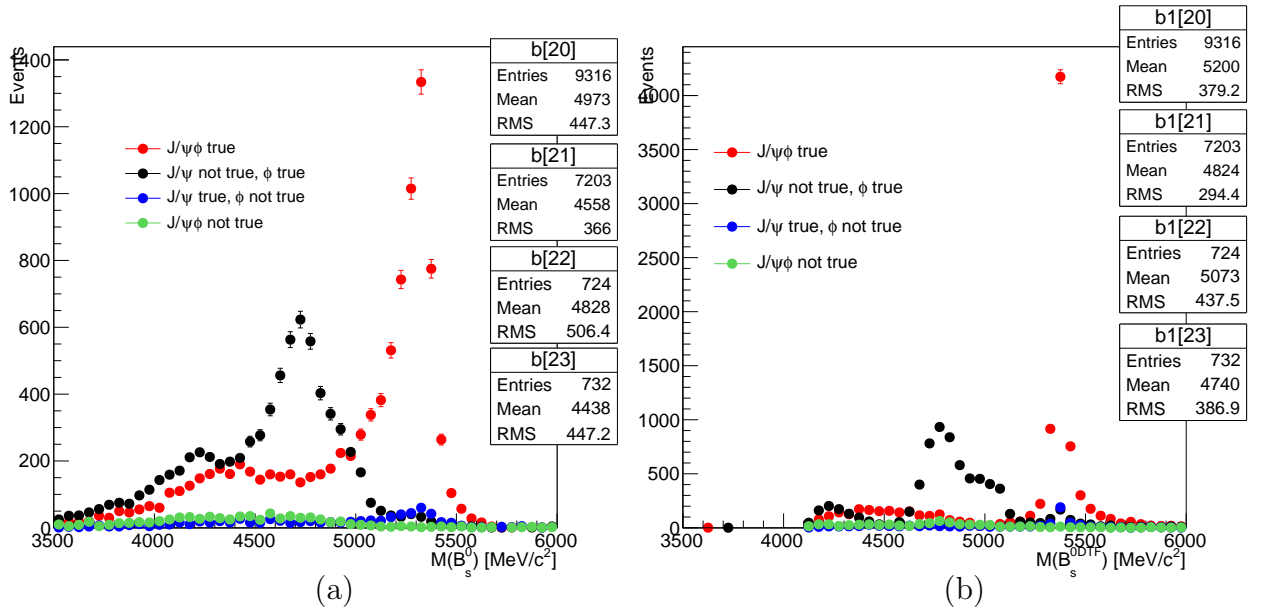


Figure 10: The background from partially reconstructed events due to missing particles from the J/ψ and/or hadronic part: (a) B_s^0 mass distribution, (b) B_s^0 mass distribution using DTF.

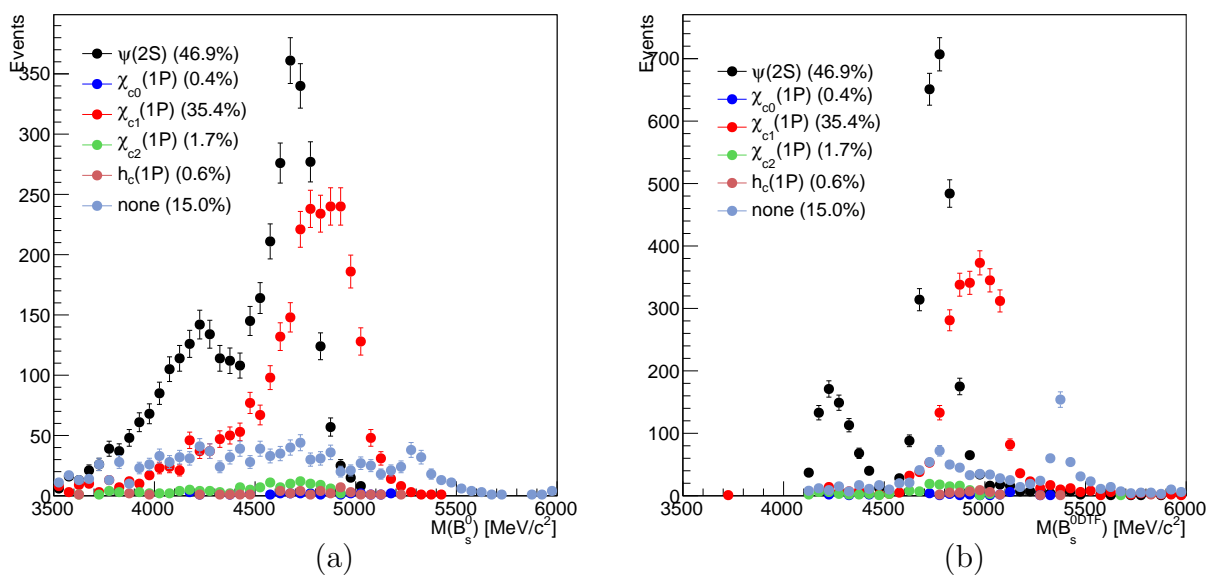


Figure 11: The J/ψ partially reconstructed background from the excited charmonium resonances for (a) B_s^0 mass distribution and (b) B_s^0 mass distribution using DTF.

287 5 Decay time resolution

288 The precision of the ϕ_s determination is dependent on the decay time resolution. As in
 289 the $B_s^0 \rightarrow J/\psi(\mu^+\mu^-)K^+K^-$ analysis [21] it could be determined from a sample of prompt
 290 $J/\psi \rightarrow e^+e^-$ events selected using the following decay time stripping and unbiased trigger
 291 lines:

- 292 • Stripping line: `StrippingBs2JpsieePhiLine`
- 293 • Unbiased triggers: `L0ElectronDecision_TOS` or `L0HadronDecision_TOS`

294 However, no $J/\psi \rightarrow e^+e^-$ peak is observed in the data (Fig. 12a), even after testing
 295 different criteria to try and isolate the signal. The J/ψ peak arises using a constraint B_s^0
 296 decay time $t > 0.3$ ps (Fig. 12b).

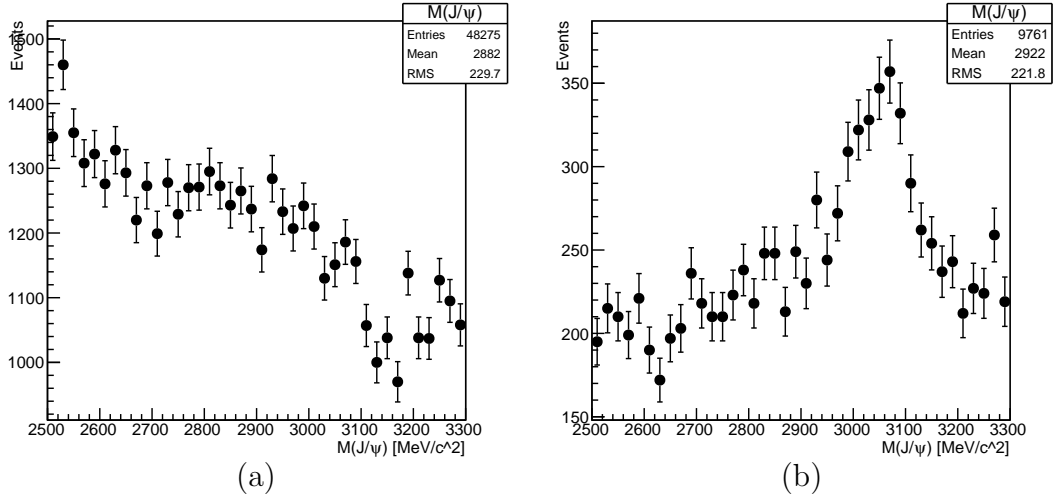


Figure 12: (a) The distribution of the $J/\psi \rightarrow e^+e^-$ invariant mass for events selected using the `Bs2JpsieePhiLine` stripping line with unbiased `L0ElectronDecision_TOS` and `L0HadronDecision_TOS` triggers. No clear sign of the $J/\psi \rightarrow e^+e^-$ decays is visible. (b) The distribution of the $J/\psi \rightarrow e^+e^-$ invariant mass for events selected using in addition the cut on the B_s^0 decay time $t > 0.3$ ps. The peak from $J/\psi \rightarrow e^+e^-$ decays is seen.

296 To solve this problem we compare the time resolution of the e^+e^- and $\mu^+\mu^-$ modes
 297 of the $B_s^0 \rightarrow J/\psi\phi$ decays, as the kinematics of these two modes are similar (see Ap-
 298 pendix D). To do this the simulated signal events from the $B_s^0 \rightarrow J/\psi(e^+e^-)\phi$ and
 299 $B_s^0 \rightarrow J/\psi(\mu^+\mu^-)K^+K^-$ channels are used. A fit was performed to the difference be-
 300 tween the true and reconstructed decay time for unbiased 2012 simulated events for
 301 both modes using the triple Gaussian resolution model. The $B_s^0 \rightarrow J/\psi(e^+e^-)\phi$ unbi-
 302 ased events pass `L0ElectronDecision_TOS` or `L0HadronDecision_TOS` triggers. In case
 303 of the $B_s^0 \rightarrow J/\psi(\mu^+\mu^-)K^+K^-$ decay, the unbiased sample includes events which passed
 304

305 Hlt2DiMuonDetachedJPsi_TOS and Hlt1DiMuonHighMass_TOS trigger lines. The parameters resulting from the fit are presented in Table 10. No sizable difference between the
 306 two modes is visible. Plots showing the fit to the difference in true and reconstructed
 307 decay time are depicted in Fig. 13. The time resolution of the $B_s^0 \rightarrow J/\psi(e^+e^-)\phi$ decay is
 308 comparable with the time resolution of the $B_s^0 \rightarrow J/\psi(\mu^+\mu^-)K^+K^-$ decay mode.

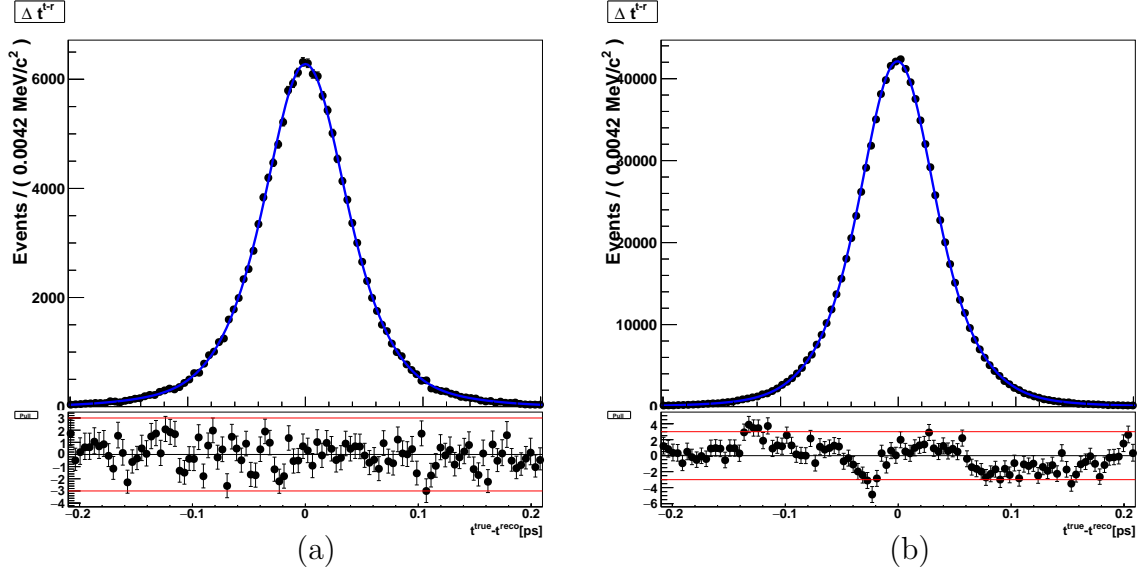


Figure 13: The distribution of $t = t^{true} - t^{reco}$ of 2012 simulated (a) $B_s^0 \rightarrow J/\psi(e^+e^-)\phi$ and (b) $B_s^0 \rightarrow J/\psi(\mu^+\mu^-)K^+K^-$ data samples. The solid blue line shows the result of a fit of the triple Gaussian resolution model. The black points with error bars represent data.

Table 10: The resolution model parameters obtained from a fit to the difference between the true and reconstructed decay time using 2012 simulated $B_s^0 \rightarrow J/\psi(e^+e^-)\phi$ and $B_s^0 \rightarrow J/\psi(\mu^+\mu^-)K^+K^-$ data samples.

	$B_s^0 \rightarrow J/\psi(e^+e^-)\phi$	$B_s^0 \rightarrow J/\psi(\mu^+\mu^-)K^+K^-$
$\mu_{\text{Gaussians}}$ [ps]	0.00010 ± 0.00012	-0.000656 ± 0.00004
σ_1 [ps]	0.0836 ± 0.0022	0.0249 ± 0.0004
σ_2 [ps]	0.0243 ± 0.0017	0.0871 ± 0.0017
σ_3 [ps]	0.0416 ± 0.0016	0.0437 ± 0.0006
f_1	0.194 ± 0.018	0.340 ± 0.017
f_2	0.207 ± 0.053	0.099 ± 0.007
f_3	0.599 ± 0.050	0.561 ± 0.017
σ_{eff} [ps]	0.0502 ± 0.0019	0.0451 ± 0.0008

309

310 6 Decay time acceptance

311 As the decay time is used in the log-likelihood fit to data, it is necessary to model the
 312 acceptance effects of the detector and selection process. To perform this we use the data
 313 driven **TISTOS** method to determine the trigger efficiencies in data and simulation. The
 314 detailed procedure of the **TISTOS** method is described in Ref. [22] but the main concept is
 315 repeated in this paper.

316 In the LHCb, the efficiency (conventionally) is a product of three terms:

$$\epsilon_{tot} = \epsilon_{rec|acc} \cdot \epsilon_{sel|rec} \cdot \epsilon_{trig|sel}, \quad (5)$$

317 where the particles in the candidate events must first lie within the detector acceptance,
 318 then be reconstructed, selected, and finally passed the trigger requirements. The trigger
 319 efficiency is defined on the final sample of selected events:

$$\epsilon_{trig} \equiv \epsilon_{trig|sel} \equiv \frac{N_{trig}}{N_{sel}}. \quad (6)$$

320 To estimate the trigger efficiency (Eq. 6) from the data, the events are splitted into two
 321 trigger categories:

- 322 • Triggered On Signal (TOS): events for which the presence of the signal is sufficient
 323 to generate a positive trigger decision;
- 324 • Triggered Independent of Signal (TIS): the "rest" of the events is sufficient to
 325 generate a positive trigger decision, where the rest of the event is defined through an
 326 operational procedure consisting in removing the signal and all detector hits belonging
 327 to it.

328 A single event can be also simultaneously TIS and TOS (TISTOS). If both the presence of
 329 the signal alone as well as the rest of the event alone are sufficient to generate a positive
 330 trigger decision. Using these event categories, the partial efficiencies are defined as

$$\epsilon_{TOS} \equiv \frac{N_{TOS}}{N_{sel}}, \quad \epsilon_{TIS} \equiv \frac{N_{TIS}}{N_{sel}}, \quad \epsilon_{TISTOS} \equiv \frac{N_{TISTOS}}{N_{sel}}. \quad (7)$$

331 Since the trigger efficiency (Eq. 6) can be expressed using the trigger categories (Eq. 7),
 332 we express ϵ_{trig} as follows:

$$\epsilon_{trig} = \frac{N_{trig}}{N_{sel}} = \frac{N_{trig}}{N_{TIS}} \times \frac{N_{TIS}}{N_{sel}} = \frac{N_{trig}}{N_{TIS}} \times \epsilon_{TIS}. \quad (8)$$

333 That the TIS efficiency of any subsample of the triggered events is the same as that of the
 334 whole sample of selected events, it can thus be measured on the TOS sample:

$$\epsilon_{TIS} \equiv \epsilon_{TIS|TOS}. \quad (9)$$

335 The trigger efficiency can now be expressed as

$$\epsilon_{trig} = \frac{N_{trig}}{N_{TIS}} \times \frac{N_{TISTOS}}{N_{TOS}}, \quad (10)$$

336 where all four quantities can be directly measured from data.

337 The trigger efficiencies of the $B_s^0 \rightarrow J/\psi\phi$ data and simulated sample are obtained for
338 two trigger categories (described in Sec. 3.4):

339 1. Unbiased: L0ElectronDecision_TOS or L0HadronDecision_TOS

340 2. Biased: Hlt1TrackAllL0Decision_TOS

341 In case of biased triggers, the one trigger is chosen since it holds a maximum number of
342 selected events in the whole biased category: 98.4% of data events and 91.3% of simulated
343 events.

344 The $B_s^0 \rightarrow J/\psi\phi$ trigger efficiencies for unbiased and biased triggers are shown in
345 Fig. 14.

346 6.1 Track reconstruction efficiency

347 The track reconstruction efficiency is computed as the ratio of the decay time distributions of
348 fully unbiased and truth matched 2012 simulated sample to the toy dataset generated with
349 the 2012 MC physics parameters. The resulting histogram is shown in Fig. 15. The efficiency
350 ratio is fitted with a quadratic function, $N(1 + \beta t + \gamma t^2)$. The obtained fit parameters of
351 the track reconstruction efficiency for $B_s^0 \rightarrow J/\psi(e^+e^-)\phi$ and $B_s^0 \rightarrow J/\psi(\mu^+\mu^-)K^+K^-$ [21]
352 decays are listed in Table 11.

Table 11: The fit parameters of the track reconstruction efficiency for $B_s^0 \rightarrow J/\psi(e^+e^-)\phi$ and $B_s^0 \rightarrow J/\psi(\mu^+\mu^-)K^+K^-$ decays.

Parameter	$B_s^0 \rightarrow J/\psi(e^+e^-)\phi$	$B_s^0 \rightarrow J/\psi(\mu^+\mu^-)K^+K^-$
N_{evt}	515	8 241
μ	6.29	6.59
RMS	3.91	3.82
χ^2/ndf	86.17/37	50.16/47
N	-0.00091±0.00021	0.09722±0.00023
β	0.06535±0.00042	0.00320±0.00183
γ	-1.556±0.112	-0.00227±0.00025

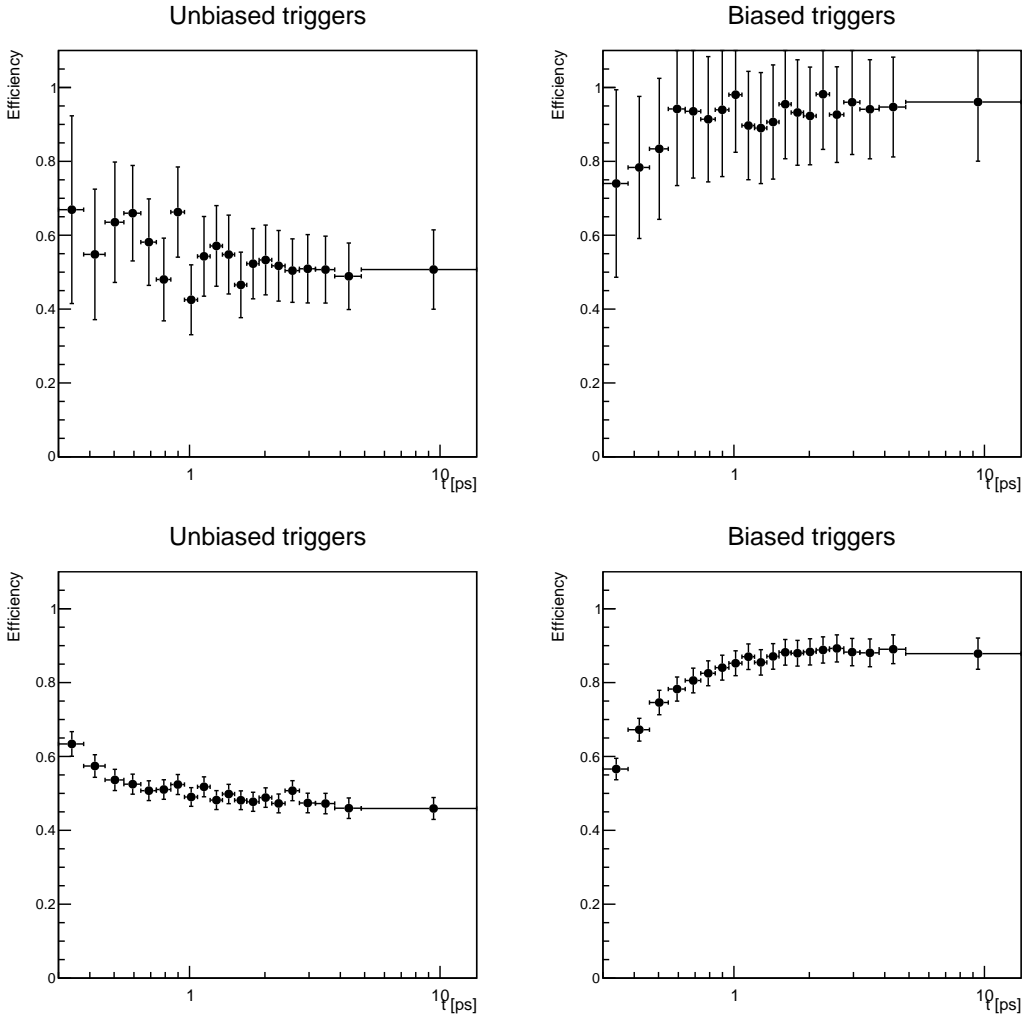


Figure 14: The trigger efficiencies of sWeighted $B_s^0 \rightarrow J/\psi\phi$ data (top) and simulation (bottom) for unbiased (left) and biased (right) triggers depending on the decay time.

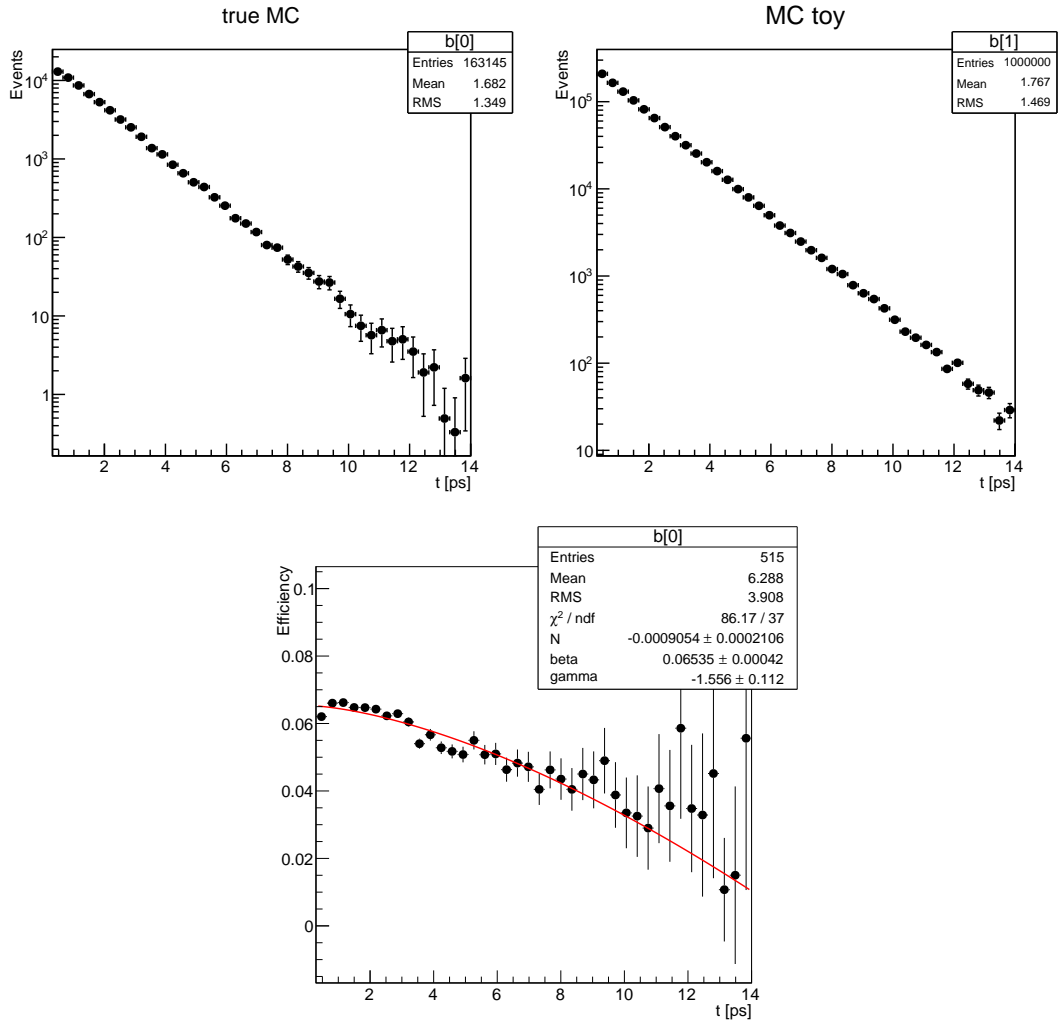


Figure 15: The ratio (bottom) of decay time distributions of completely unbiased and truth matched events in 2012 MC (top left) to toy events generated with the 2012 MC physics parameters (top right).

353 **7 Angular acceptance**

354 Effects of angular acceptance are modeled with normalization weights (see Ref. [12],
355 Sec. 3.3). The normalization weights are obtained from fully simulated signal sample from
356 the Sim08 production (Sec. 3.2), as described in Sec. 7.1.

357 **7.1 Normalization weights from full simulation**

358 The angular acceptance normalization weights determined with the Sim08 Monte Carlo
359 samples are shown in Table 12. Table 13 shows the correlations between the errors of
360 the weights. In Table 14 the 10 weights corresponding to 10 terms of the PDF (Eq. 1)
361 are split by running year. As no significant difference is observed between the two years
362 (Fig. 17), the weights are calculated and normalized separately for each running year and
363 then they are combined to the one final set of weights of Table 12. The one-dimentional
364 projections of the angular efficiency functions are shown in Fig. 16. No reweighting of the
365 final state kinematics has been applied since the B_s^0 and K momentum and K^+K^- mass
366 distribution in simulation are observed to well reproduce those in data (Fig. 18).

Table 12: The uncorrected angular acceptance weights for the sum of 2011 and 2012 Sim08 simulated sample.

k		ξ_k/ξ_1
1	(00)	0.9796 ± 0.0010
2	()	1.0206 ± 0.0012
3	(⊥⊥)	1.0208 ± 0.0012
4	(⊥)	0.0005 ± 0.0013
5	(0)	0.0007 ± 0.0009
6	(0⊥)	0.0014 ± 0.0009
7	(SS)	0.9929 ± 0.0008
8	(S)	0.0002 ± 0.0012
9	(S⊥)	-0.0003 ± 0.0012
10	(S0)	-0.0038 ± 0.0027

Table 13: The correlations between the uncorrected angular acceptance weights for the sum of 2011 and 2012 Sim08 simulated sample.

k	1(00)	2()	3(⊥⊥)	4(⊥)	5(0)	6(0⊥)	7(SS)	8(S)	9(S⊥)	10(S0)
1(00)	1	-0.67	-0.69		0.27		-0.05			
2()		1	0.40		0.21		0.24			
3(⊥⊥)			1		0.31		0.18			
4(⊥)				1		-0.09				
5(0)					1		0.30			
6(0⊥)						1				
7(SS)							1			
8(S)								1		0.14
9(S⊥)									1	
10(S0)										1

Table 14: The uncorrected angular acceptance weights for the 2011 and 2012 Sim08 simulated samples.

k	Sim08 2011		Sim08 2012	Diff(σ)
	(00)	ξ_k/ξ_1	ξ_k/ξ_1	
1	(00)	0.9803±0.0014	0.9786±0.0015	-0.8
2	()	1.0197±0.0017	1.0219±0.0019	+0.9
3	(⊥⊥)	1.0203±0.0016	1.0214±0.0018	+0.5
4	(⊥)	0.0013±0.0018	-0.0005±0.0020	+0.7
5	(0)	0.0008±0.0012	0.0004±0.0014	-0.2
6	(0⊥)	0.0017±0.0012	0.0011±0.0013	-0.3
7	(SS)	0.9909±0.0011	0.9953±0.0012	+2.7
8	(S)	-0.0018±0.0016	0.0025±0.0018	+1.8
9	(S⊥)	0.0006±0.0016	-0.0013±0.0018	-0.8
10	(S0)	-0.0055±0.0036	-0.0017±0.0040	+0.7

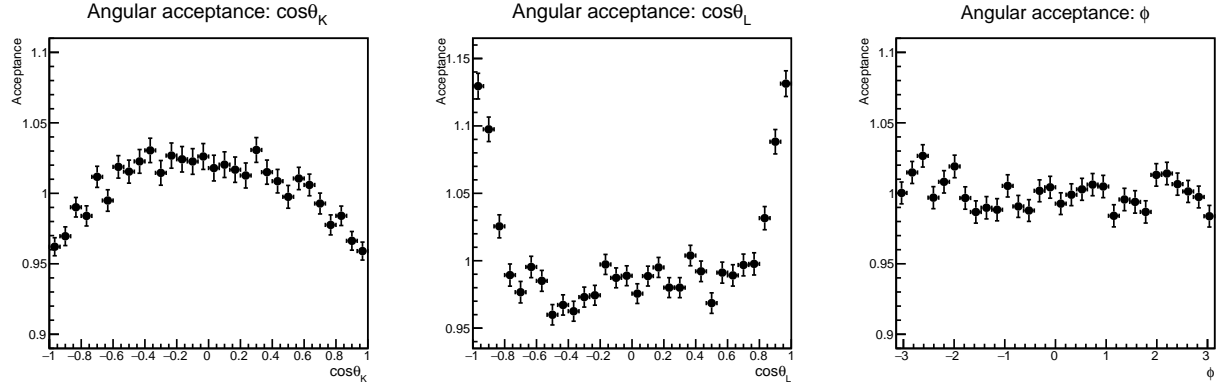


Figure 16: The angular acceptance projections as function of the three helicity angles for full simulated $B_s^0 \rightarrow J/\psi(e^+e^-)\phi$ sample.

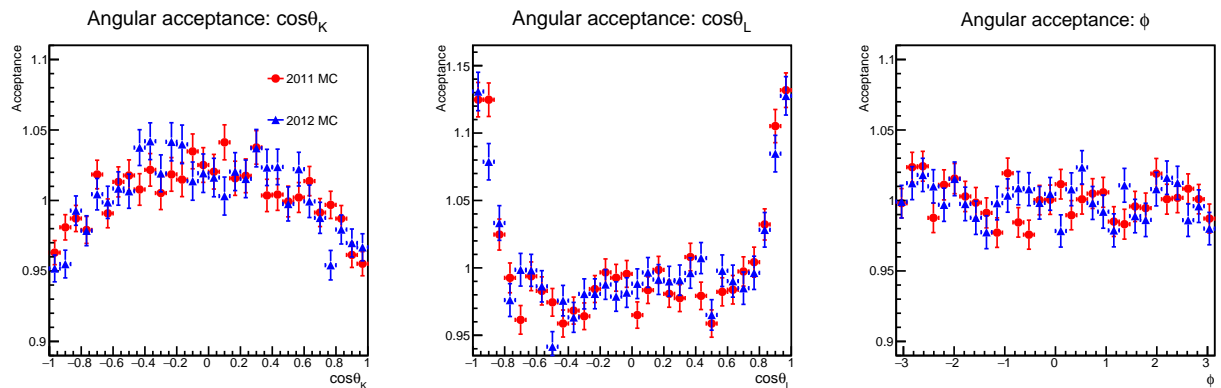


Figure 17: The angular acceptance projections as function of the three helicity angles for simulated $B_s^0 \rightarrow J/\psi(e^+e^-)\phi$ events. 2011 and 2012 samples are compared.

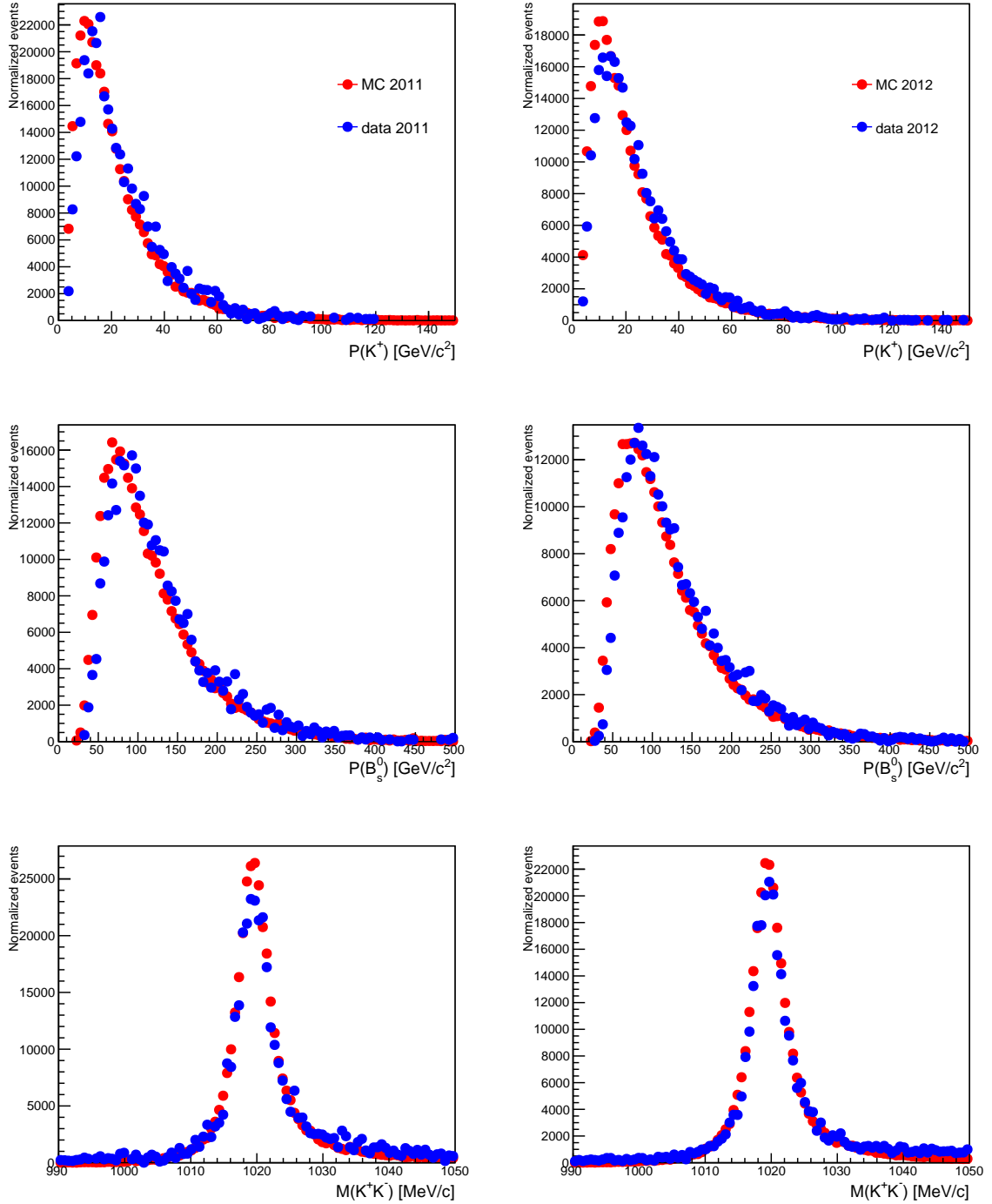


Figure 18: The comparison between the kinematical variables of $B_s^0 \rightarrow J/\psi(e^+e^-)\phi$ signal events in sWeighted data (blue) and simulation data (red) for 2011 (left) and 2012 (right) run periods.

367 8 Angular resolution

368 The angular resolution is defined as the difference between true and reconstructed angle
 369 in simulated sample. The one-dimensional projections of the three angular resolutions are
 370 shown in Fig. 19. For angles θ_K and θ_L , the used fitted model is a sum of three Gaussian
 371 functions, while for ϕ a double Gaussian plus a Voigtian component is required in order to
 372 better model the large non-Gaussian tails. The parameters determined from these fits are
 373 reported in Table 15. It has been shown in Ref. [21] that there is no correlation between
 374 the resolution of the three angles. Two-dimensional distributions of the helicity angles are
 375 shown in Fig. 20.

376 Based upon studies performed in Ref. [21], the effect from the angular resolution is
 377 negligible. It is considered as a source of systematic uncertainty in Sec. 11.3.

Table 15: The fit results to the angular resolution distributions for each of the helicity angles taken from $B_s^0 \rightarrow J/\psi(e^+e^-)\phi$ simulated signal sample for 2011 and 2012 run periods. The last row shows the effective Gaussian resolution computed for θ_K and θ_L .

Parameter	3 Gaussian	3 Gaussian	2 Gaussian+Voigtian
	θ_L	θ_K	ϕ
$\sigma_1[\text{mrad}]$	20.61 ± 0.18	12.66 ± 0.06	17.35 ± 0.11
$\sigma_2[\text{mrad}]$	7.083 ± 0.08	21.42 ± 0.08	36.03 ± 0.36
$\sigma_3[\text{mrad}]$	62.54 ± 0.35	47.71 ± 0.80	38.30 ± 0.77
$\sigma_4[\text{mrad}]$	-	-	83.00 ± 1.20
f_1	0.3902 ± 0.0026	0.3926 ± 0.0058	0.4970 ± 0.0073
f_2	0.1545 ± 0.0031	0.5632 ± 0.0052	0.4027 ± 0.0056
f_3	0.4553 ± 0.0040	0.0442 ± 0.0078	0.1003 ± 0.0091
$\sigma_{eff}[\text{mrad}]$	44.21 ± 0.34	20.54 ± 0.45	-

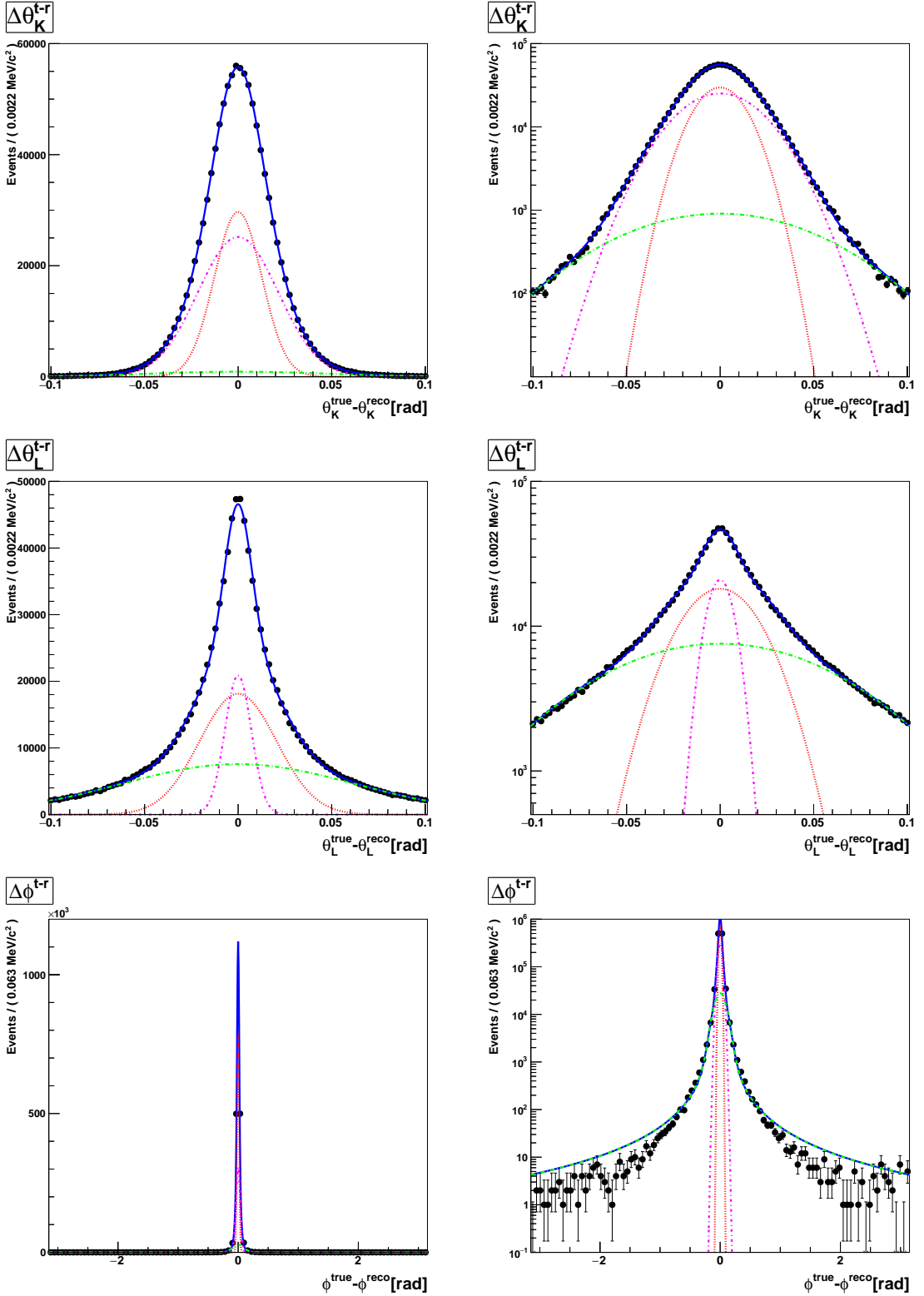


Figure 19: The distributions of the difference between the true and reconstructed angle from the simulated sample of $B_s^0 \rightarrow J/\psi(e^+e^-)\phi$ decays. A fit is superimposed in each distribution. The right hand side shows the logarithmic scale plots.

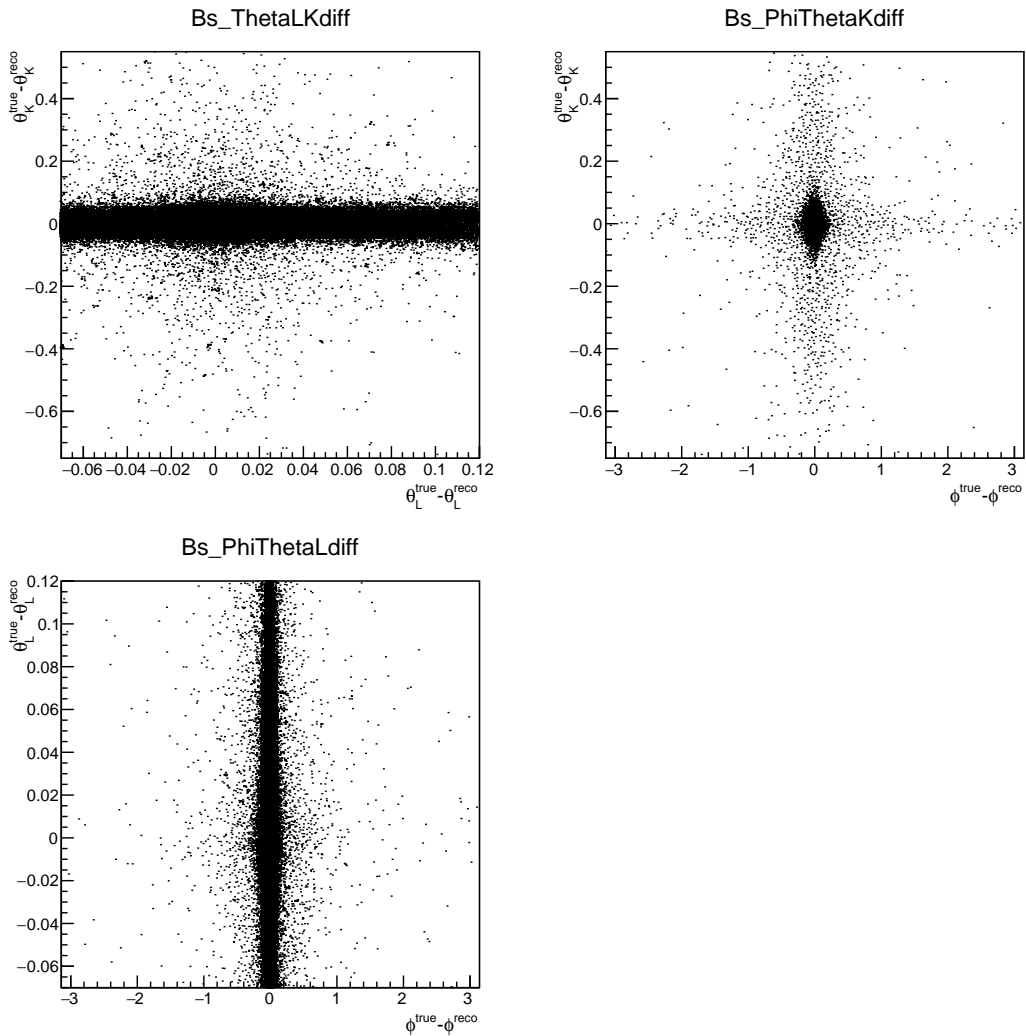


Figure 20: The two-dimensional distributions of the helicity angle resolutions obtained from simulated data. The units are in radians in all cases.

378 9 Flavour tagging

379 The flavour of the B_s^0 candidate at production state is inferred by two independent classes
 380 of flavour tagging algorithms, the opposite-side (OS) tagger and the same-side kaon (SSK)
 381 tagger, which exploit specific features of the incoherent production of $b\bar{b}$ quark pairs in pp
 382 collisions. Each tagging algorithm gives a tag decision and a mistag probability. The tag
 383 decision takes three values: +1, -1, or 0, correspond to B_s^0 , \bar{B}_s^0 , or untagged B_s^0 meson,
 384 respectively. The fraction of events in the sample with a non-zero tagging decision gives
 385 the efficiency of the tagger, ε . The mistag probability, η , is estimated event-by-event, and
 386 it represents the probability that the algorithm assigns a wrong tag decision to the event.
 387 It is calibrated using data samples of several flavour specific B^0 and B^+ decays, to obtain
 388 the corrected mistag probability, ω . The corrected mistag probability determines the
 389 square dilution factor of the tagger, $\langle \mathcal{D}^2 \rangle = \langle (1 - 2\omega)^2 \rangle$. The $\langle \mathcal{D}^2 \rangle$ rescales the efficiency
 390 of the tagger to quantify the fraction of the sample equivalent to perfectly tagged events.
 391 The effective efficiency, called tagging power, is given by the product of the efficiency and
 392 the square dilution factor, $\varepsilon \langle \mathcal{D}^2 \rangle$.

393 By means of flavour conservation of the strong interaction, the OS tagger consists of a
 394 few algorithms [23]. They infer the signal production flavour from the decay products of
 395 the b -hadron produced by the other b quark in the event, by using the charge of muons
 396 or electrons from second B_s^0 in semileptonic decays, the net charge of the opposite-side
 397 displaced vertex, and the charge of the kaon from opposite-side $b \rightarrow c \rightarrow s$ transitions. All
 398 algorithms are combined to provide a single OS tagging response. The cut-based selection
 399 of the tagging candidates and the neural networks that calculate the mistag probabilities
 400 are optimized for the analysis of the full 2011 and 2012 datasets by using a data sample of
 401 $B^+ \rightarrow J/\psi K^+$ decays. As a result, the OS algorithm has tagging power of $(3.42 \pm 0.08)\%$
 402 in $B_s^0 \rightarrow J/\psi(e^+e^-)\phi$ data, with a tagging efficiency of $(36.31 \pm 0.45)\%$.

403 The SSK algorithm deduces the signal production flavour by exploiting charge-flavour
 404 correlations of the kaon produced during its fragmentation. A selection for the identifi-
 405 cation of the tagging kaon candidate is based on a neural network (NNetSSK) [24]. The
 406 NNetSSK algorithm [25] has a tagging efficiency of $(62.83 \pm 0.45)\%$ and a tagging power of
 407 $(2.02 \pm 0.05)\%$ in $B_s^0 \rightarrow J/\psi(e^+e^-)\phi$ data.

408 The mistag probabilities, η^{alg} ($\text{alg} = \text{OS}, \text{SSK}$), are calibrated on data to get the
 409 corrected probabilities ω^{alg} and $\bar{\omega}^{\text{alg}}$, for B_s^0 and \bar{B}_s^0 , respectively:

$$410 \quad \omega^{\text{alg}} = \left(p_0^{\text{alg}} + \frac{\Delta p_0^{\text{alg}}}{2} \right) + \left(p_1^{\text{alg}} + \frac{\Delta p_1^{\text{alg}}}{2} \right) (\eta^{\text{alg}} - \langle \eta^{\text{alg}} \rangle) \quad \text{for an initial } B_s^0 \text{ event,}$$

$$410 \quad \bar{\omega}^{\text{alg}} = \left(p_0^{\text{alg}} - \frac{\Delta p_0^{\text{alg}}}{2} \right) + \left(p_1^{\text{alg}} - \frac{\Delta p_1^{\text{alg}}}{2} \right) (\eta^{\text{alg}} - \langle \eta^{\text{alg}} \rangle) \quad \text{for an initial } \bar{B}_s^0 \text{ event,} \quad (11)$$

411 where p_i^{alg} ($i = 0, 1$) are the calibration parameters, averaged for B_s^0 and \bar{B}_s^0 events;
 412 Δp_i^{alg} , called mistag asymmetries, are the difference between the calibration parameters
 413 as measured for B_s^0 and \bar{B}_s^0 . The $\langle \eta^{\text{ang}} \rangle$ is the average of the mistag distribution of the

⁴¹⁴ $B_s^0 \rightarrow J/\psi(e^+e^-)\phi$ data, unfolded from background with the sPlot technique [17] by using
⁴¹⁵ the $J/\psi\phi$ mass as discriminating variable (Fig. 21). The parameters used in Eq. 11 are
reported in Table 16. They are the results of the standard calibration provided by the

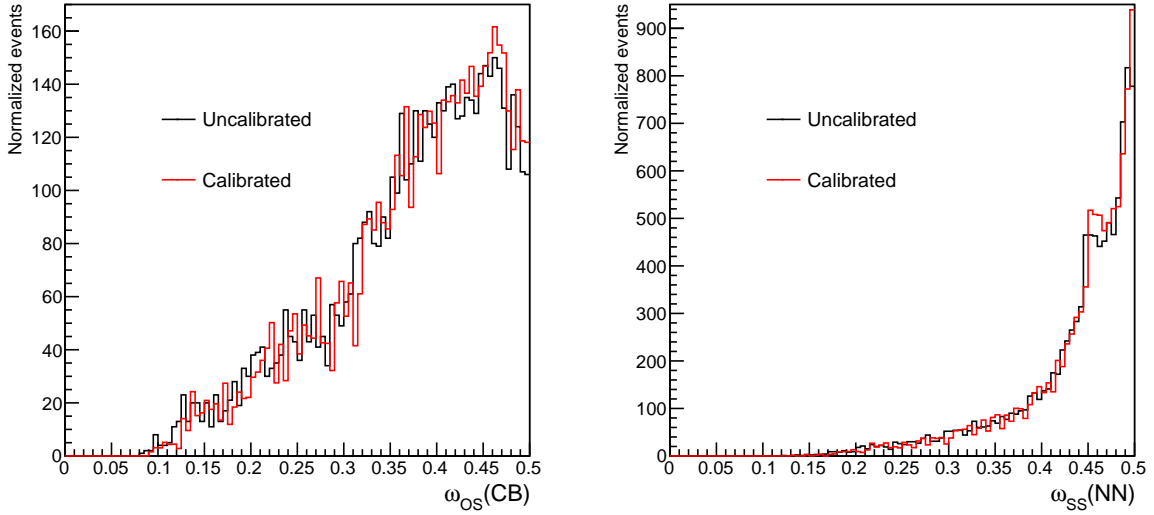


Figure 21: The OS (left) and SSK (right) mistag distributions for $B_s^0 \rightarrow J/\psi(e^+e^-)\phi$ signal events before (black) and after (red) the calibration.

⁴¹⁶ Flavour Tagging group [26, 27]: p_i^{OS} are the combinations of calibration in data samples
⁴¹⁷ of several decays ($B^+ \rightarrow J/\psi K^+$, $B^+ \rightarrow D^0\pi^+$, $B^0 \rightarrow J/\psi K^{*0}$, $B^0 \rightarrow D^{*-}\mu^+X$ and
⁴¹⁸ $B_s^0 \rightarrow D_s^-\pi^+$); the OS mistag asymmetries are measured with $B^+ \rightarrow J/\psi K^+$, $B^+ \rightarrow D^0\pi^+$
⁴¹⁹ and $B^0 \rightarrow J/\psi K^{*0}$ decays; p_i^{SSK} are extracted by measuring the B_s^0 flavour oscillations
⁴²⁰ in a sample of $B_s^0 \rightarrow D_s^-\pi^+$ decays; the SSK mistag asymmetries are determined from a
⁴²¹ sample of prompt $D_s^+ \rightarrow \phi\pi^+$ decays, reweighted to match the B_s^0 kinematic distributions.
⁴²² Systematic uncertainties of calibration parameters address the portability of the calibrations
⁴²³ from the control samples to $B_s^0 \rightarrow J/\psi(e^+e^-)\phi$ data; they are dominated by the effect of
⁴²⁴ the different kinematic distributions between the decay modes used in calibration and
⁴²⁵ the $B_s^0 \rightarrow J/\psi(e^+e^-)\phi$ signal data. Such systematic errors are independent from the
⁴²⁶ flavour decision, and they mainly cancel when computing the mistag asymmetries. Their
⁴²⁷ small contribution - approximately 10% (20%) of the systematic error of p_0 (p_1) for $\Delta p_0/2$
⁴²⁸ ($\Delta p_1/2$) - are directly included in the single errors of the mistag asymmetries reported in
⁴²⁹ Table 16.

⁴³⁰ The $B_s^0 \rightarrow J/\psi(e^+e^-)\phi$ data sample is split in four independent subsamples, according
⁴³¹ to the tag decisions: exclusive OS tagged events ($q^{\text{OS}} \neq 0$ and $q^{\text{SSK}} = 0$), referred to as "OS-
⁴³² only" events; exclusive SSK tagged events ($q^{\text{OS}} = 0$ and $q^{\text{SSK}} \neq 0$), referred to as "SSK-only"
⁴³³ events; OS and SSK tagged events ($q^{\text{OS}} \neq 0$ and $q^{\text{SSK}} \neq 0$), referred to as "OS&SSK" events;
⁴³⁴ and finally, untagged events ($q^{\text{OS}} = q^{\text{SSK}} = 0$), which are about 22% and 26% of the data and
⁴³⁵ simulation samples, respectively. The fractions, the efficiencies, and the tagging powers of

Table 16: The parameters used in Eq. 11 to calibrate the per-event mistag probabilities. When two uncertainties are quoted, the first one is statistical and the second one is systematic.

Parameter	OS	SSK
$\langle \eta \rangle$	0.3751	0.4373
$p_0 - \langle \eta \rangle$	$0.0062 \pm 0.0019 \pm 0.0040$	$0.005 \pm 0.004 \pm 0.003$
$\Delta p_0/2$	0.0070 ± 0.0006	-0.0079 ± 0.0007
p_1	$0.982 \pm 0.007 \pm 0.034$	$0.976 \pm 0.071 \pm 0.057$
$\Delta p_1/2$	0.033 ± 0.006	0.0035 ± 0.0111

437 the tagged categories OS-only, SSK-only and OS&SSK as measured for $B_s^0 \rightarrow J/\psi(e^+e^-)\phi$
438 signal candidates from full 2011 and 2012 datasets and from full simulation sample are
439 reported in Tables 17 and 18, respectively. The total tagging efficiency and tagging power
440 of data sample are $(75.70 \pm 0.68)\%$ and $(5.20 \pm 0.10)\%$, respectively. In case of simulated
441 data, the total tagging efficiency and tagging power are $(74.73 \pm 0.13)\%$ and $(5.38 \pm 0.02)\%$,
442 respectively. The flavour tagging performance obtained using simulation is in agreement
443 with flavour tagging performance for data within statistical uncertainty.

Table 17: The summary of the tagging efficiency (ε), square dilution factor (\mathcal{D}^2) and tagging power ($\varepsilon\mathcal{D}^2$) for the different categories of tagger, obtained from $B_s^0 \rightarrow J/\psi(e^+e^-)\phi$ **signal candidates from full 2011 and 2012 data samples** after the tagging calibration. The column "Fraction" reports the fraction of events in each category out of the all tagged events.

Category	Fraction(%)	$\varepsilon(\%)$	\mathcal{D}^2	$\varepsilon\mathcal{D}^2(\%)$
OS-only	17.0	12.87 ± 0.31	0.0977 ± 0.0025	1.26 ± 0.05
SSK-only	52.0	39.39 ± 0.46	0.0315 ± 0.0013	1.24 ± 0.04
OS&SSK	31.0	23.44 ± 0.40	0.1152 ± 0.0020	2.70 ± 0.08
Total	100	75.70 ± 0.68	0.0687 ± 0.0033	5.20 ± 0.10

444 The time dependent angular decay rate without taking into account any resolution
445 and acceptance effect, $R(t, \Omega | q^{\text{alg}}, \eta^{\text{alg}})$, can be written as:

$$R(t, \Omega | q^{\text{alg}}, \eta^{\text{alg}}) = (1 + q^{\text{OS}}(1 - 2\omega^{\text{OS}}))(1 + q^{\text{SSK}}(1 - 2\bar{\omega}^{\text{SSK}}))R(t, \Omega | B_s^0)$$

446

$$+ (1 - q^{\text{OS}}(1 - 2\bar{\omega}^{\text{OS}}))(1 - q^{\text{SSK}}(1 - 2\bar{\omega}^{\text{SSK}}))R(t, \Omega | \bar{B}_s^0), \quad (12)$$

447 where $R(t, \Omega | B_s^0)$ and $R(t, \Omega | \bar{B}_s^0)$ are the time dependent angular decay rates for an initial
448 B_s^0 and \bar{B}_s^0 , respectively; ω and $\bar{\omega}$ are derived from Eq. 11. By considering $q^{\text{OS}}=0$ and
449 $q^{\text{SSK}}=0$ as a special tagging decision, Eq. 12 provides a unified form of the time dependent
450 angular decay rate for any of the four independent categories considered, i.e. no matter a
451 tagging decision is (or both decisions are) zero.

Table 18: The summary of the tagging efficiency (ε), square dilution factor (\mathcal{D}^2) and tagging power ($\varepsilon\mathcal{D}^2$) for the different categories of tagger, obtained from $B_s^0 \rightarrow J/\psi(e^+e^-)\phi$ **signal candidates from full simulated data sample** after the tagging calibration has been applied. The column "Fraction" reports the fraction of events in each category out of the all tagged events.

Category	Fraction(%)	$\varepsilon(\%)$	\mathcal{D}^2	$\varepsilon\mathcal{D}^2(\%)$
OS-only	16.7	12.46 ± 0.06	0.0995 ± 0.0006	1.24 ± 0.01
SSK-only	54.0	40.33 ± 0.09	0.0347 ± 0.0003	1.40 ± 0.01
OS&SSK	29.3	21.94 ± 0.07	0.1249 ± 0.0005	2.74 ± 0.02
Total	100	74.73 ± 0.13	0.0720 ± 0.0008	5.38 ± 0.02

452 9.1 OS calibration on $B^+ \rightarrow J/\psi(\mu^+\mu^-)K^+$ and $B^+ \rightarrow J/\psi(e^+e^-)K^+$ decays

454 Since the final state of $B_s^0 \rightarrow J/\psi\phi$ decay includes e^+e^- particles the OS calibrations on
455 $B^+ \rightarrow J/\psi(\mu^+\mu^-)K^+$ and $B^+ \rightarrow J/\psi(e^+e^-)K^+$ are applied. As determined in Sec. 9
456 the OS algorithm on $B^+ \rightarrow J/\psi(\mu^+\mu^-)K^+$ has tagging power of $(3.42 \pm 0.08)\%$ in $B_s^0 \rightarrow$
457 $J/\psi(e^+e^-)\phi$ data, with a tagging efficiency of $(36.31 \pm 0.45)\%$. In case electron mode
458 of $B^+ \rightarrow J/\psi K^+$, the OS algorithm has tagging power of $(3.20 \pm 0.07)\%$ and a tagging
459 efficiency of $(36.74 \pm 0.45)\%$ in $B_s^0 \rightarrow J/\psi(e^+e^-)\phi$ data.

460 The same SSK algorithm (Sec. 9) has been applied to both channels.

461 To get the corrected probabilities ω^{OS} and $\bar{\omega}^{OS}$, the mistag probability, η^{OS} , is calibrated
462 on data as defined in Eq. 11. The mistag distributions of the sWeighted $B_s^0 \rightarrow J/\psi\phi$ data
463 before and after two OS calibrations are shown in Fig. 22. The parameters reported in
464 Table 19 are the results of the calibration provided by the Flavour Tagging group [26, 28]
465 for muon and electron modes of $B^+ \rightarrow J/\psi K^+$ decay.

Table 19: The parameters used in Eq. 11 to calibrate the per-event mistag probabilities for OS calibration. When two uncertainties are quoted, the first one is statistical and the second one is systematic.

Parameter	$B^+ \rightarrow J/\psi(\mu^+\mu^-)K^+$	$B^+ \rightarrow J/\psi(e^+e^-)K^+$
$\langle \eta \rangle$	0.3751	0.3789
$p_0 - \langle \eta \rangle$	$0.0062 \pm 0.0019 \pm 0.0040$	0.0086 ± 0.0021
$\Delta p_0/2$	0.0070 ± 0.0006	0.0083 ± 0.0021
p_1	$0.982 \pm 0.007 \pm 0.034$	0.931 ± 0.021
$\Delta p_1/2$	0.033 ± 0.006	0.0115 ± 0.0205

466 The $B_s^0 \rightarrow J/\psi(e^+e^-)\phi$ dataset is divided in four independent subsamples as described
467 in Sec. 9. The fractions, the efficiencies, and the tagging powers calculated for OS calibration

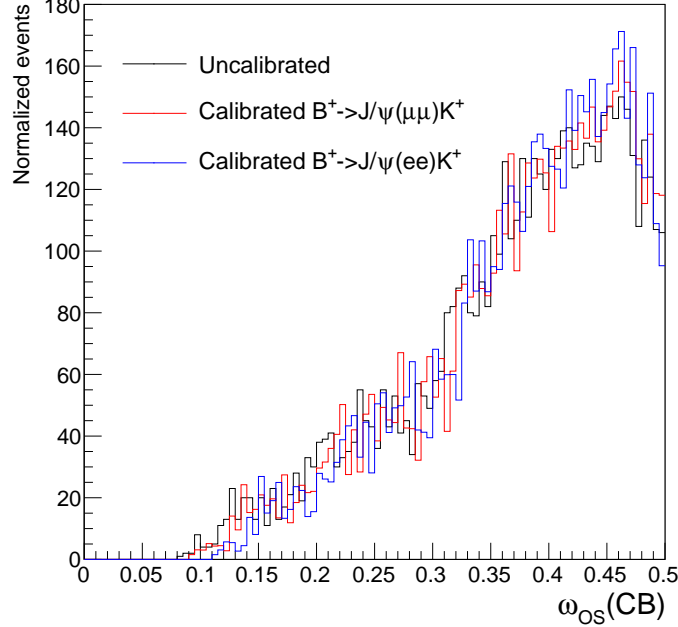


Figure 22: The OS mistag distributions for $B_s^0 \rightarrow J/\psi \phi$ signal events before (black) and after the calibration on $B^+ \rightarrow J/\psi(\mu^+\mu^-)K^+$ (red) and $B^+ \rightarrow J/\psi(e^+e^-)K^+$ (blue).

on $B^+ \rightarrow J/\psi(\mu^+\mu^-)K^+$ and $B^+ \rightarrow J/\psi(e^+e^-)K^+$ as measured for $B_s^0 \rightarrow J/\psi(e^+e^-)\phi$ signal candidates from full 2011 and 2012 datasets and from full simulation sample are reported in Table 17, 20 and Table 18, 21, respectively. The total tagging efficiency and tagging power of data sample are $(75.70 \pm 0.68)\%$ and $(5.20 \pm 0.10)\%$ with OS calibration on muon mode of $B^+ \rightarrow J/\psi K^+$ and $(75.80 \pm 0.68)\%$ and $(4.98 \pm 0.10)\%$ for OS calibration on $B^+ \rightarrow J/\psi K^+$ with electron final state. In case of simulated data, the total tagging efficiency and tagging power are $(74.73 \pm 0.13)\%$ and $(5.38 \pm 0.02)\%$ with OS calibration on $B^+ \rightarrow J/\psi(\mu^+\mu^-)K^+$ and $(74.90 \pm 0.13)\%$ and $(5.17 \pm 0.02)\%$ with OS calibration on $B^+ \rightarrow J/\psi(e^+e^-)K^+$ decay. The flavour tagging performance calculated for OS calibration on electron mode of $B^+ \rightarrow J/\psi K^+$ slightly decreases the tagging performance of $B_s^0 \rightarrow J/\psi(e^+e^-)\phi$ signal events. It is considered as a source of systematic uncertainty in Sec. 11.6.

Table 20: The summary of the tagging efficiency (ε), square dilution factor (\mathcal{D}^2) and tagging power ($\varepsilon\mathcal{D}^2$) for the different categories of tagger, obtained from $B_s^0 \rightarrow J/\psi(e^+e^-)\phi$ **signal candidates from full 2011 and 2012 data samples** after the OS tagging calibration on $B_s^0 \rightarrow J/\psi(e^+e^-)\phi$ has been applied. The column "Fraction" reports the fraction of events in each category out of the all tagged events.

Category	Fraction(%)	$\varepsilon(\%)$	\mathcal{D}^2	$\varepsilon\mathcal{D}^2(\%)$
OS-only	17.1	12.98 ± 0.32	0.0901 ± 0.0024	1.17 ± 0.05
SSK-only	51.5	39.06 ± 0.46	0.0315 ± 0.0013	1.23 ± 0.04
OS&SSK	31.4	23.76 ± 0.40	0.1086 ± 0.0020	2.58 ± 0.08
Total	100	75.80 ± 0.68	0.0657 ± 0.0033	4.98 ± 0.10

Table 21: The summary of the tagging efficiency (ε), square dilution factor (\mathcal{D}^2) and tagging power ($\varepsilon\mathcal{D}^2$) for the different categories of tagger, obtained from $B_s^0 \rightarrow J/\psi(e^+e^-)\phi$ **signal candidates from full simulated data sample** after the OS tagging calibration on $B_s^0 \rightarrow J/\psi(e^+e^-)\phi$ has been applied. The column "Fraction" reports the fraction of events in each category out of the all tagged events.

Category	Fraction(%)	$\varepsilon(\%)$	\mathcal{D}^2	$\varepsilon\mathcal{D}^2(\%)$
OS-only	16.9	12.65 ± 0.06	0.0917 ± 0.0006	1.16 ± 0.01
SSK-only	55.7	40.03 ± 0.09	0.0347 ± 0.0003	1.39 ± 0.01
OS&SSK	27.4	22.22 ± 0.07	0.1179 ± 0.0005	2.62 ± 0.02
Total	100	74.90 ± 0.13	0.0690 ± 0.0008	5.17 ± 0.02

480 10 Results of likelihood fit

481 Table 22 shows the $B_s^0 \rightarrow J/\psi(e^+e^-)\phi$ final results of the fit to 3 fb^{-1} of LHCb dataset
 482 including decay time and angular acceptance effect, decay time resolution and fixed flavour
 483 tagging calibration. A blind string has been applied in the fit for Γ_s , $\Delta\Gamma_s$ and ϕ_s . The
 484 correlation matrix of the fit is shown in Table 23. The projections of the fit result on the
 485 decay time and helicity angle distributions are shown in Fig. 23 (Preliminary).

Table 22: The results of the unbinned maximum likelihood fit to the selected $B_s^0 \rightarrow J/\psi(e^+e^-)\phi$ candidates including all acceptance and resolution effects. The tagging calibration parameters and Δm_s are Gaussian constrained in the fit. The values for Γ_s , $\Delta\Gamma_s$ and ϕ_s are blinded. The uncertainty is statistical. Preliminary

Parameter	Fit result and error
$\Gamma_s [\text{ps}^{-1}]$	$X.XXX \pm 0.0057$
$\Delta\Gamma_s [\text{ps}^{-1}]$	$X.XXX \pm 0.0155$
A_\perp^2	0.2750 ± 0.0121
A_0^2	0.5025 ± 0.0088
$\delta_{ } [\text{rad}]$	3.0092 ± 0.1759
$\delta_\perp [\text{rad}]$	3.1086 ± 0.3686
F_S	0.0735 ± 0.0167
$\delta_S [\text{rad}]$	-0.1093 ± 0.0801
$\phi_s [\text{rad}]$	$X.XXX \pm 0.1548$
λ	0.9836 ± 0.0261
$\Delta m_s [\text{ps}^{-1}]$	18.176 ± 0.147

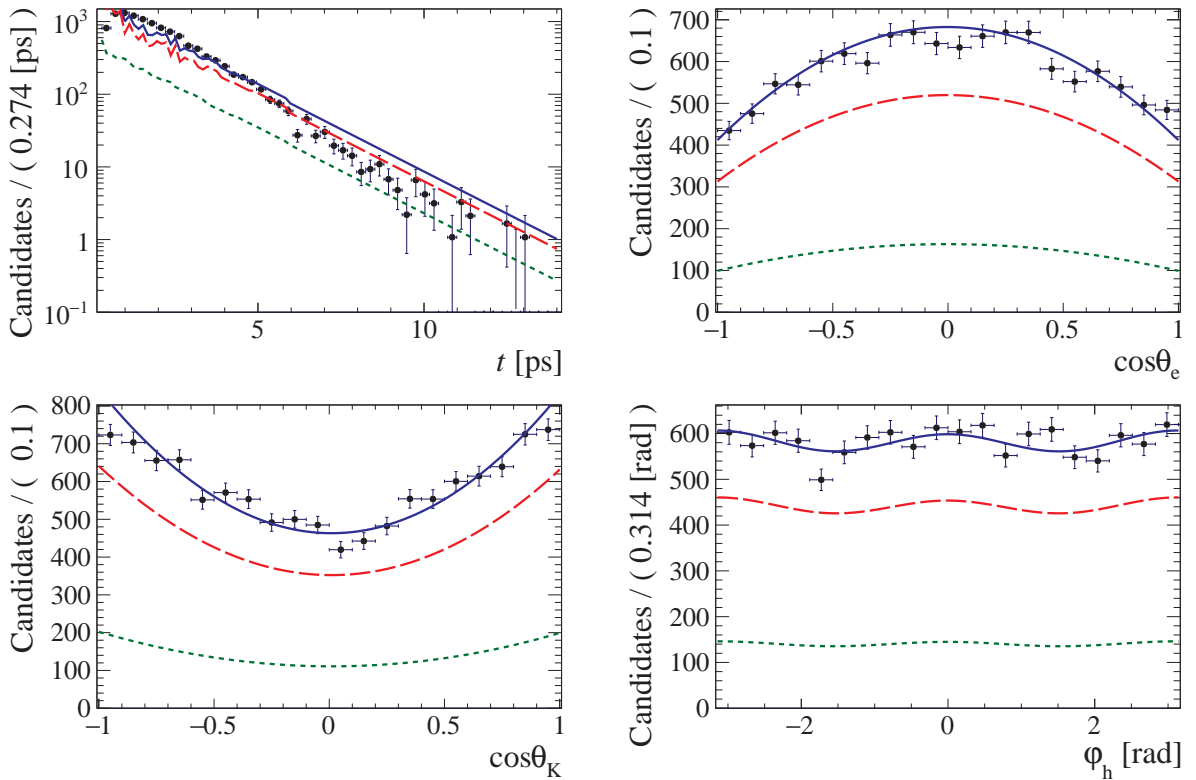


Figure 23: The decay time and helicity-angle distributions for $B_s^0 \rightarrow J/\psi(e^+e^-)\phi$ reconstructed candidates (data points) with the one-dimensional projections of the PDF at the maximum likelihood fit. The solid blue line shows the total signal contribution, which is composed of CP -even (long dashed red), CP -odd (short-dashed green) and S-wave (dash-dotted purple) (not seen) contributions. Preliminary.

Table 23: the statistical correlation matrix from nominal fit. Preliminary

	Γ	$\Delta\Gamma$	A_{\perp}^2	A_0^2	δ_{\parallel}	δ_{\perp}	F_S	δ_S	Δm_s	ϕ_s	λ	ω_{P1}^{OS}	ω_{P0}^{OS}	ω_{P1}^{SS}	ω_{P0}^{SS}
Γ	1.00	-0.31	0.22	-0.18	0.02	0.01	0.13	0.02	0.01	0.03	0.02	-0.00	0.00	-0.00	0.00
$\Delta\Gamma$	1.00	-0.54	0.52	-0.00	0.01	-0.14	-0.02	0.01	-0.01	-0.02	0.00	-0.00	0.00	-0.00	-0.00
A_{\perp}^2	1.00	-0.52	0.17	0.06	0.01	0.02	0.03	0.04	0.04	0.04	-0.00	-0.00	-0.00	-0.00	0.00
A_0^2	1.00	0.02	-0.01	-0.00	0.00	-0.01	-0.03	0.00	0.00	0.00	0.00	0.00	0.00	0.00	-0.00
δ_{\parallel}															
δ_{\perp}															
F_S															
δ_S															
Δm_s															
ϕ_s															
λ															
ω_{P1}^{OS}															
ω_{P0}^{OS}															
ω_{P1}^{SS}															
ω_{P0}^{SS}															

486 11 Systematic uncertainties

487 All systematics are described below and a summary is reported in Table 24. The tagging
488 parameters are allowed to float in the fit (Gaussian constrained within their uncertainty)
489 and thus the systematic uncertainties due to those is propagated into the statistical
490 uncertainties reported on physics parameters.

491 11.1 $M(J/\psi(e^+e^-)\phi)$ mass model

492 To calculate a new set of event weights obtained from new $M(J/\psi(e^+e^-)\phi)$ fit model.

493 11.2 Angular acceptance

494 To add the description of iterative weighting method.

495 11.3 Angular resolution

496 To add the toy studies of the angular resolution.

497 11.4 Decay time resolution

498 11.5 Trigger efficiency

499 11.6 Flavour tagging

500 The difference between tagging parameters obtained from OS calibration on $B^+ \rightarrow$
501 $J/\psi(\mu^+\mu^-)K^+$ and $B^+ \rightarrow J/\psi(e^+e^-)K^+$ is assigned as the systematic uncertainty.

502 11.7 Length and momentum scale

503 The uncertainty on the LHCb length scale is estimated to be at most 0.020% [29], which
504 translates directly in an uncertainty on Γ_s , $\Delta\Gamma_s$ and Δm_s of 0.020% with other parameters
505 being unaffected. The momentum scale uncertainty is at most 0.022% [29]. As it affects
506 both the reconstructed momentum and mass of the B_s^0 meson, it cancels to a large extent
507 and the resulting effect on Γ_s and $\Delta\Gamma_s$ is negligible.

508 11.8 Contribution from Λ_b^0 decays

509 11.9 Fit bias

510 A possible bias of the fitting procedure is investigated by generating and fitting many
511 simulated pseudo-experiments of equivalent size to the data sample, generated with physics
512 parameters close to those obtained in the nominal fit.

⁵¹³ **11.10 Further checks**

⁵¹⁴ Additional checks will perform by repeating the nominal fit to data in bins of year of data
⁵¹⁵ taking, magnet polarity.

Table 24: Statistical and systematic uncertainties. The uncertainty for ϕ_s from the fit bias will need to be re-evaluated post-unblinding.

Source	Γ_s [ps ⁻¹]	$\Delta\Gamma_s$ [ps ⁻¹]	A_{\perp}^2	A_0^2	δ_{\parallel} [rad]	δ_{\perp} [rad]	ϕ_s [rad]	λ
Stat. uncert.	0.0057	0.0155	0.0121	0.0088	0.1759	0.3686	0.1548	0.0261
Mass model								
Ang. acc.								
Ang. resol.								
Time resol.								
Trigger eff.								
Flav. tag.								
Length, mom. scales								
A_b^0 background								
Fit bias								
Quad. sum of syst.								
Total uncertainties								

516 12 Conclusion

517 We have presented the tagged, time dependent angular analysis of $11\,645 \pm 114$ $B_s^0 \rightarrow$
 518 $J/\psi(e^+e^-)\phi$ signal candidates with $J/\psi \rightarrow e^+e^-$ and in the $M(K^+K^-)$ region around the
 519 $\phi(1020)$ meson. These were recorded in 3 fb^{-1} of pp collision data collected by the LHCb
 520 detector during 2011 and 2012 years. The effective decay time resolution and effective
 521 tagging power are 50.2 fs and 5.2% , respectively. The analysis provides access to a number
 522 of different physics parameters including the CP -violating phase, average decay width
 523 and decay width difference of the B_s^0 system as well as the transversely amplitudes and
 524 strong phases of the decay. The final results are reported in Table 25. This is the first
 525 measurement of the CP content of the $B_s^0 \rightarrow J/\psi(e^+e^-)\phi(K^+K^-)$ decay and first time
 526 that ϕ_s and $\Delta\Gamma_s$ have been measured in final state containing the $J/\psi \rightarrow e^+e^-$ decay.
 527 These measurements will contribute to increased precision in the global average of the B_s^0
 528 mixing parameters.

Table 25: The results of the unbinned maximum likelihood fit to the selected $B_s^0 \rightarrow J/\psi(e^+e^-)\phi$ candidates including all acceptance and resolution effects. The tagging calibration parameters and Δm_s are Gaussian constrained in the fit. The values for $\Delta\Gamma_s$ and ϕ_s are blinded. The uncertainty is statistical.

Parameter	Fit result and error
$\Gamma_s [\text{ps}^{-1}]$	$X.XXX \pm 0.0057$
$\Delta\Gamma_s [\text{ps}^{-1}]$	$X.XXX \pm 0.0155$
A_\perp^2	0.2750 ± 0.0121
A_0^2	0.5025 ± 0.0088
$\delta_\parallel [\text{rad}]$	3.0092 ± 0.1759
$\delta_\perp [\text{rad}]$	3.1086 ± 0.3686
F_S	0.0735 ± 0.0167
$\delta_S [\text{rad}]$	-0.1093 ± 0.0801
$\phi_s [\text{rad}]$	$X.XXX \pm 0.1548$
λ	0.9836 ± 0.0261
$\Delta m_s [\text{ps}^{-1}]$	18.176 ± 0.147

529 13 To-do list

- 530 1. Add comparison plots of kinematic variables for $B_s^0 \rightarrow J/\psi(\mu^+\mu^-)\phi$ and $B_s^0 \rightarrow$
531 $J/\psi(e^+e^-)\phi$
- 532 2. Complete systematic studies
- 533 3. Perform final fit projections of the decay time and helicity angle

534 **Appendices**

535 **A Analysis code**

536 The DecayTreeTuple are made running DaVinci v37r2p4 on the grid. We use Erasmus
537 v10r2. The various steps are:

- 538 1. "DTT" with Phys/B2CCtuples/python/BuBdBs_NTUPLE_maker_(2011,2012).py
539 (to change), running DaVinci v37r2p4;
- 540 2. "tupleA" with Phys/B2CCtuples/src/sel1Candidate_Bs2JpsiPhi.C, revision 166293
541 (to change);
542 /eos/lhcb/user/v/vbatozsk/B0s2JpsieePhi/
543 DVNtuple_Bs2JpsieePhiStrip21_TupleBsDetached_RD11_tupleA_new.root
544 /eos/lhcb/user/v/vbatozsk/B0s2JpsieePhi/
545 DVNtuple_Bs2JpsieePhiStrip21_TupleBsDetached_RD11_tupleA_new.root
- 546 3. "tupleB" with Phys/B2CCtuples/src/CreateNtupleB.C revision 164683 (to change);
547 /eos/lhcb/user/v/vbatozsk/B0s2JpsieePhi/
548 DVNtuple_Bs2JpsieePhiStrip21_TupleBsDetached_RD11_tupleB.root
549 /eos/lhcb/user/v/vbatozsk/B0s2JpsieePhi/
550 DVNtuple_Bs2JpsieePhiStrip21_TupleBsDetached_RD11_tupleB.root
- 551 4. Add physics weights to MC tuples: Phys/B2CCtuples/python/mcTuples.py;
- 552 5. "tupleC" Phys/B2CCtuples/python/makeNTupleC.py;
- 553 6. "final fitting tuple", where the mass sWeights are recomputed dividing
554 the samples in the categories mentioned in the note, with Phys-
555 Fit/P2VV/examples/createB2CCFitNTuple.py. (to check)

556 The location of the final NTuples are /castor/cern.ch/user/j/jleerdam/JpsiKK_fitNTuples/fitNTupl
557 /castor/cern.ch/user/j/jleerdam/JpsiKK_fitNTuples/fitNTuple_peakBkg_2011_2012_Reco14
558 _20140116.root. (to change)

559 **B Data/MC comparison**

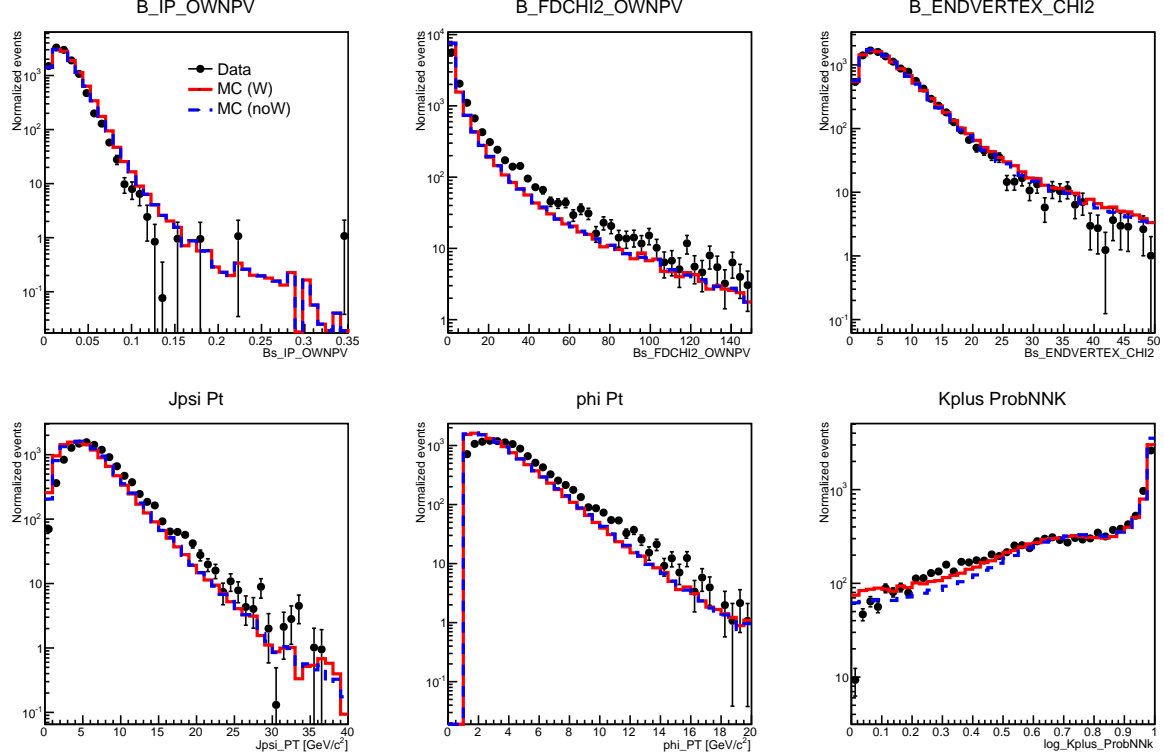


Figure 24: Data(_sPlot)/MC comparison for $B_s^0 \rightarrow J/\psi(e^+e^-)\phi$. All distributions are in logarithmic scale.

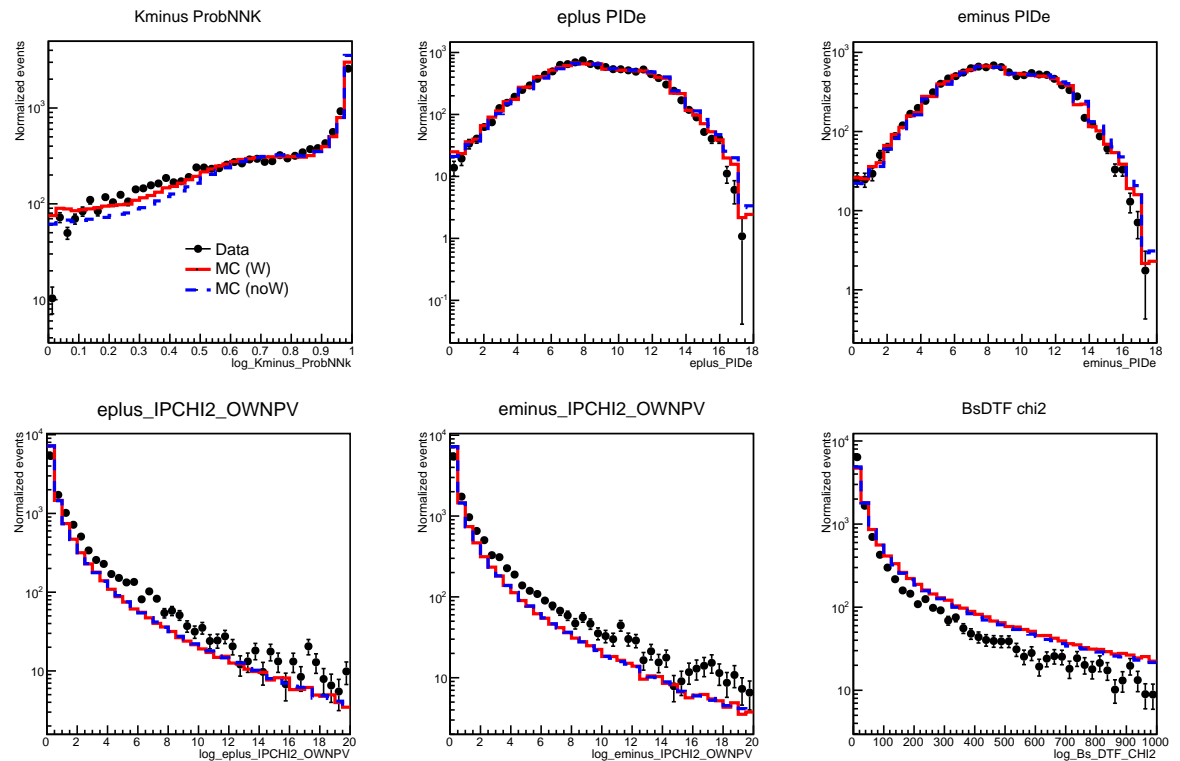


Figure 25: Data(_sPlot)/MC comparison for $B_s^0 \rightarrow J/\psi(e^+e^-)\phi$. All distributions are in logarithmic scale.

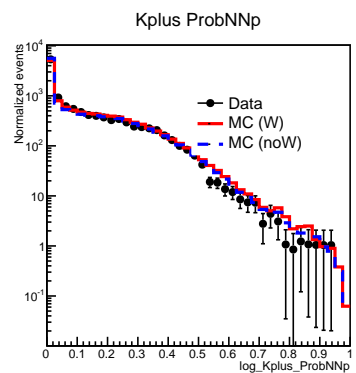


Figure 26: Data(_sPlot)/MC comparison for $B_s^0 \rightarrow J/\psi(e^+e^-)\phi$. All distributions are in logarithmic scale.

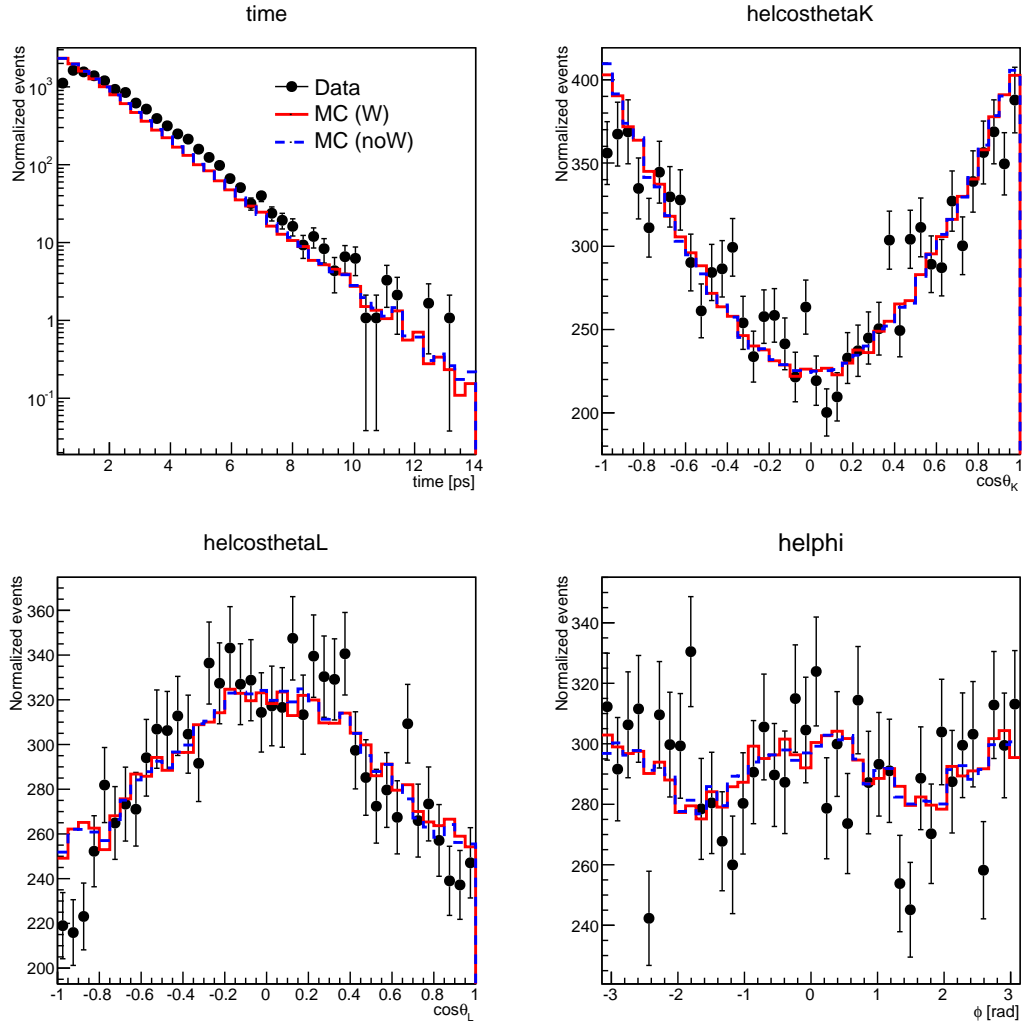


Figure 27: Data(_sPlot)/MC comparison for $B_s^0 \rightarrow J/\psi(e^+e^-)\phi$. The decay time distribution are in logarithmic scale.

560 **C BDT training**

561 **C.1 Boosted Decision Tree**

562 This section includes the details of the BDT used for the final step of selection (Sec. 3.6).
 563 The list of variables used is shown in Table 5. Plots showing the distributions of the input
 variables from TMVA are shown in Figure 31.

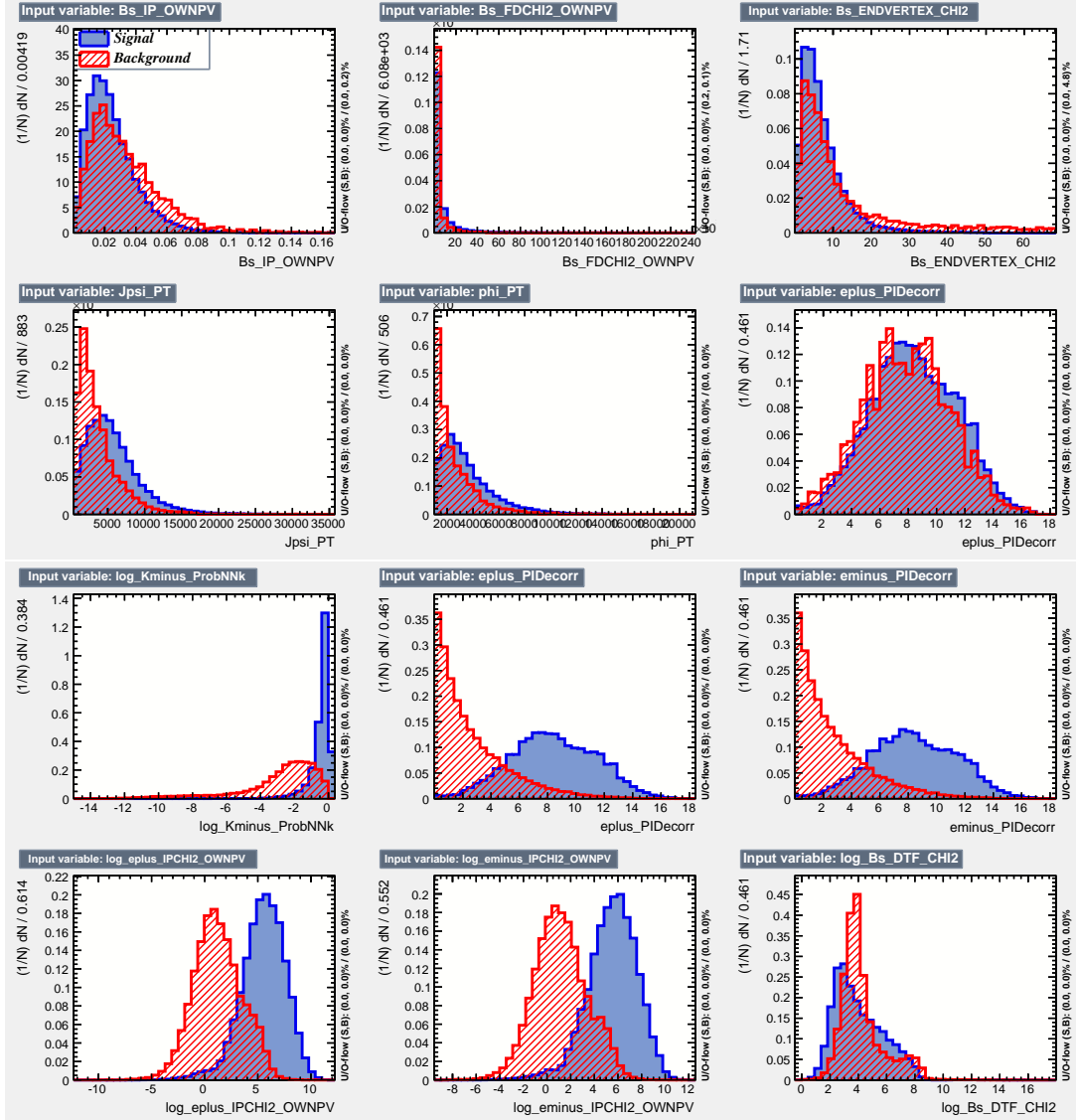


Figure 28: Input variable distributions for signal (blue) and background (red) for the 2012 BDT training.

565 **C.2 Peaking background**

566 This section includes the details of second BDT used to reduce background under B_s^0
 567 mass peak (Sec. 3.7). The list of variables used is shown in Table 6. Plots showing the
 distributions of the input variables from TMVA are shown in Figure 29.

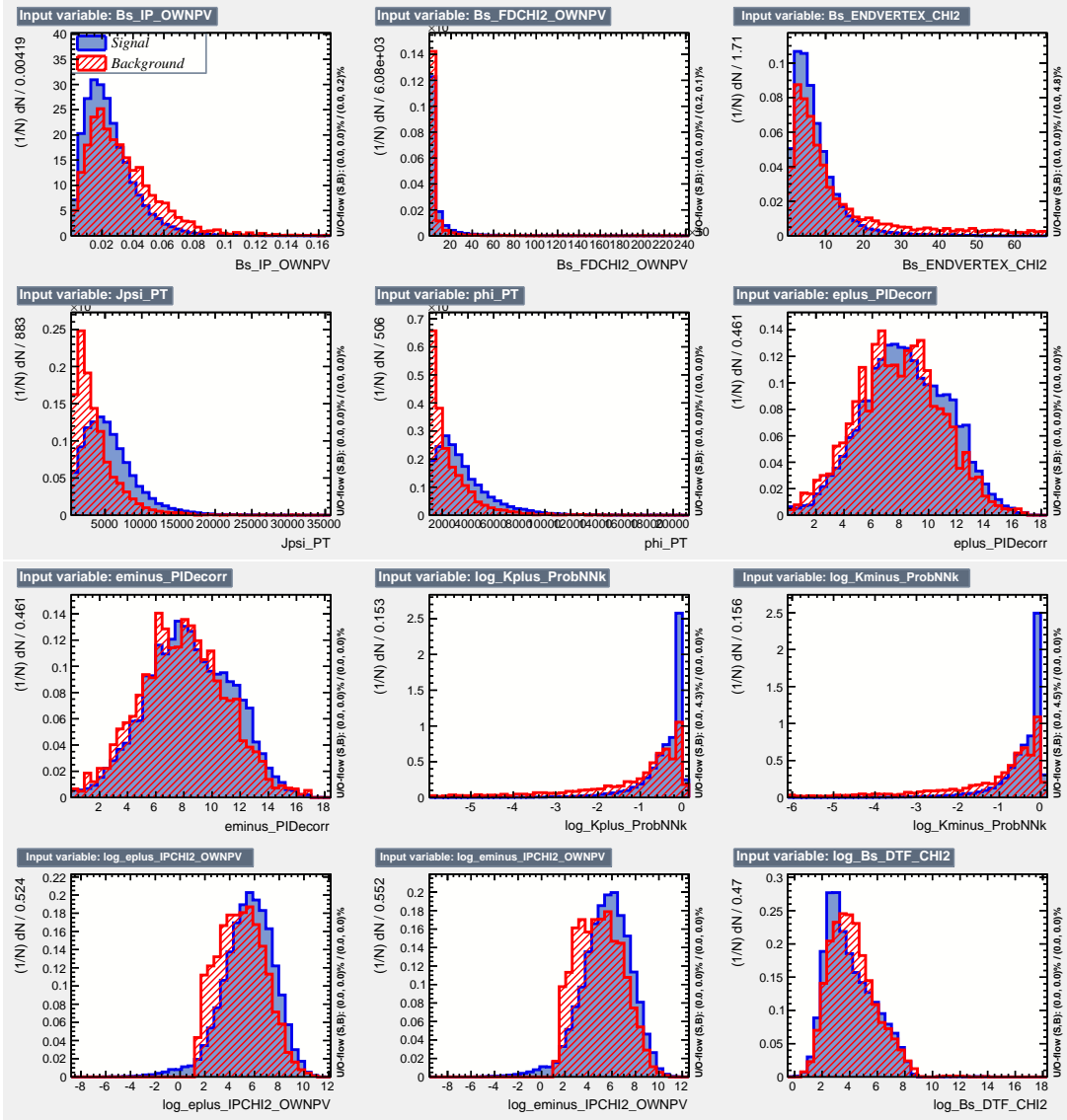


Figure 29: Input variable distributions for signal (blue) and background (red) for the 2012 BDT training.

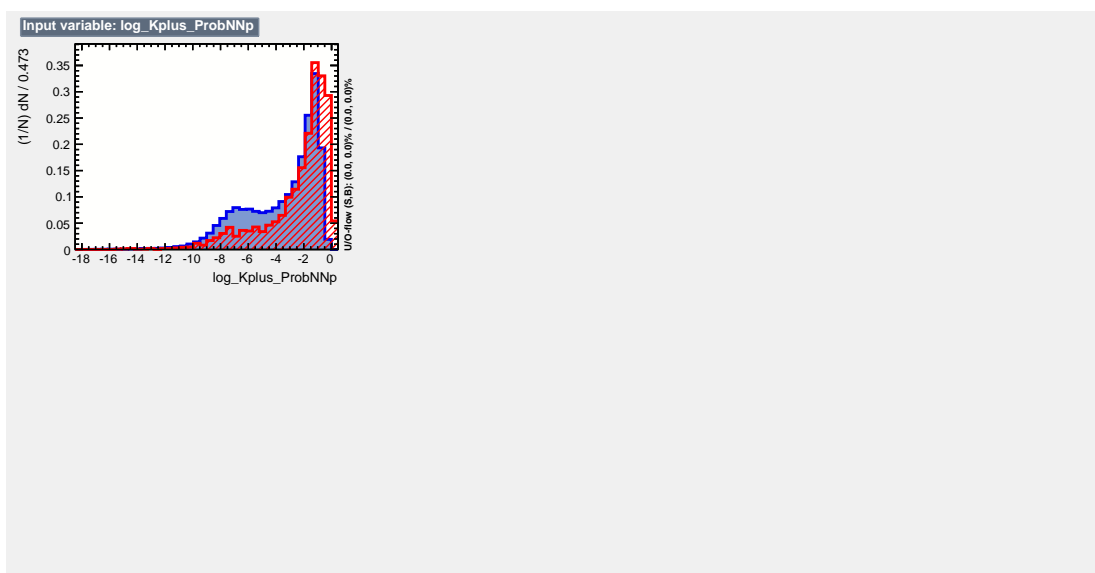


Figure 30: Input variable distributions for signal (blue) and background (red) for the 2012 BDT training.

569 **D Comparison of $B_s^0 \rightarrow J/\psi(\mu^+\mu^-)K^+K^-$ and $B_s^0 \rightarrow$**

570 $J/\psi(e^+e^-)\phi$ distributions

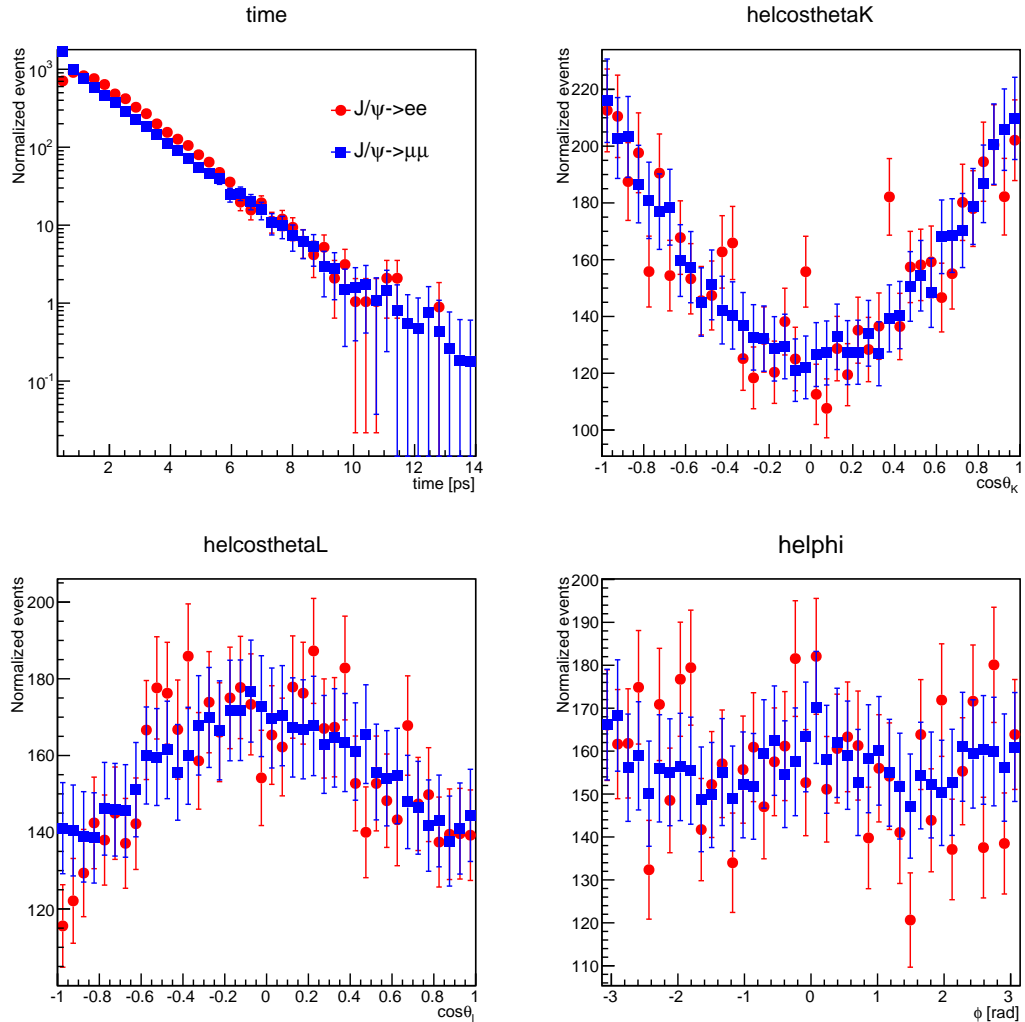


Figure 31: Plot of the decay time and helicity angles for sWeighted $B_s^0 \rightarrow J/\psi(e^+e^-)\phi$ data (red) and sWeighted $B_s^0 \rightarrow J/\psi(\mu^+\mu^-)K^+K^-$ data (blue).

571 References

- 572 [1] M. Kobayashi and T. Maskawa, *CP Violation in the Renormalizable Theory of Weak*
573 *Interaction*, Prog. Theor. Phys. **49** (1973) 652.
- 574 [2] N. Cabibbo, *Unitary Symmetry and Leptonic Decays*, Phys. Rev. Lett. **10** (1963) 531,
575 [,648(1963)].
- 576 [3] J. Charles *et al.*, *Predictions of selected flavour observables within the Standard Model*,
577 Phys. Rev. **D84** (2011) 033005, arXiv:1106.4041, with updated results and plots
578 available at <http://ckmfitter.in2p3.fr>.
- 579 [4] A. J. Buras, *Flavour Theory: 2009*, PoS **EPS-HEP2009** (2009) 024,
580 arXiv:0910.1032.
- 581 [5] C.-W. Chiang *et al.*, *New Physics in $B_s^0 \rightarrow J/\psi\phi$: A General Analysis*, JHEP **04**
582 (2010) 031, arXiv:0910.2929.
- 583 [6] LHCb, R. Aaij *et al.*, *Precision measurement of CP violation in $B_s^0 \rightarrow J/\psi K^+K^-$*
584 *decays*, Phys. Rev. Lett. **114** (2015), no. 4 041801, arXiv:1411.3104.
- 585 [7] ATLAS, G. Aad *et al.*, *Flavor tagged time-dependent angular analysis of the $B_s \rightarrow$*
586 *$J/\psi\phi$ decay and extraction of $\Delta\Gamma_s$ and the weak phase ϕ_s in ATLAS*, Phys. Rev. **D90**
587 (2014), no. 5 052007, arXiv:1407.1796.
- 588 [8] CMS, V. Khachatryan *et al.*, *Measurement of the CP-violating weak phase ϕ_s and the*
589 *decay width difference $\Delta\Gamma_s$ using the $Bs0J/(1020)$ decay channel in pp collisions at*
590 *$\sqrt{s}=8$ TeV*, Phys. Lett. **B757** (2016) 97, arXiv:1507.07527.
- 591 [9] CDF, T. Aaltonen *et al.*, *Measurement of the Bottom-Strange Meson Mixing Phase*
592 *in the Full CDF Data Set*, Phys. Rev. Lett. **109** (2012) 171802, arXiv:1208.2967.
- 593 [10] D0, V. M. Abazov *et al.*, *Measurement of the CP-violating phase $\phi_s^{J/\psi\phi}$ using the*
594 *flavor-tagged decay $B_s^0 \rightarrow J/\psi\phi$ in 8 fb^{-1} of $p\bar{p}$ collisions*, Phys. Rev. **D85** (2012)
595 032006, arXiv:1109.3166.
- 596 [11] LHCb, R. Aaij *et al.*, *Measurement of CP violation and the B_s^0 meson decay width*
597 *difference with $B_s^0 \rightarrow J/\psi K^+K^-$ and $B_s^0 \rightarrow J/\psi\pi^+\pi^-$ decays*, Phys. Rev. **D87** (2013),
598 no. 11 112010, arXiv:1304.2600.
- 599 [12] LHCb, R. Aaij *et al.*, *Tagged time-dependent analysis of $B_s^0 \rightarrow J/\psi K^+K^-$ and*
600 *$B_s^0 \rightarrow J/\psi\pi^+\pi^-$ decays with 1.0 fb^{-1}* , LHCb-ANA-2012-067.
- 601 [13] X. Liu, W. Wang, and Y. Xie, *Penguin pollution in $B \rightarrow J/\psi V$ decays and impact*
602 *on the extraction of the $B_s - \bar{B}_s$ mixing phase*, Phys. Rev. **D89** (2014), no. 9 094010,
603 arXiv:1309.0313.

- 604 [14] LHCb, M. Borsato *et al.*, *Angular analysis of $B^0 \rightarrow K^{*0}e^+e^-$ at LHCb with 3fb^{-1}* ,
 605 LHCb-ANA-2014-009.
- 606 [15] A. Hocker *et al.*, *TMVA - Toolkit for Multivariate Data Analysis*, PoS **ACAT** (2007) 040, [arXiv:physics/0703039](https://arxiv.org/abs/physics/0703039).
- 608 [16] Y. Xie, *Formalism for Simulation-based Optimization of Measurement Errors in High*
 609 *Energy Physics*, [arXiv:0901.3305](https://arxiv.org/abs/0901.3305).
- 610 [17] M. Pivk and F. R. Le Diberder, *sPlot: A statistical tool to unfold data distributions*,
 611 Nucl. Instrum. Meth. **A555** (2005) 356, [arXiv:physics/0402083](https://arxiv.org/abs/physics/0402083).
- 612 [18] J. J. Olivero and R. L. Longbothum, *Empirical fits to the voigt line width: A brief*
 613 *review*, Journal of Quantitative Spectroscopy and Radiative Transfer **17** (1977), no. 2
 614 233 .
- 615 [19] Particle Data Group, K. A. Olive *et al.*, *Review of particle physics*, Chin. Phys. **C38**
 616 (2014) 090001, and 2015 update.
- 617 [20] T. Sjöstrand, S. Mrenna, and P. Skands, *PYTHIA 6.4 physics and manual*, JHEP **05**
 618 (2006) 026, [arXiv:hep-ph/0603175](https://arxiv.org/abs/hep-ph/0603175).
- 619 [21] LHCb, R. Aaij *et al.*, *Flavour tagged time-dependent angular analysis of $B_s^0 \rightarrow$*
 620 *$J/\psi K^+K^-$ decays in the low K^+K^- mass range*, LHCb-ANA-2014-039.
- 621 [22] S. Tolk *et al.*, *Data driven trigger efficiency determination at LHCb*, LHCb-PUB-
 622 2014-039.
- 623 [23] LHCb, R. Aaij *et al.*, *Opposite-side flavour tagging of B mesons at the LHCb experi-*
 624 *ment*, Eur. Phys. J. **C72** (2012) 2022, [arXiv:1202.4979](https://arxiv.org/abs/1202.4979).
- 625 [24] LHCb, *Optimization and calibration of the same-side kaon tagging algorithm using*
 626 *hadronic B_s^0 decays in 2011 data*, LHCb-CONF-2012-033, CERN-LHCb-CONF-2012-
 627 033.
- 628 [25] LHCb, R. Aaij *et al.*, *A new algorithm for identifying the flavour of B_s^0 mesons at*
 629 *LHCb*, JINST **11** (2016), no. 05 P05010, [arXiv:1602.07252](https://arxiv.org/abs/1602.07252).
- 630 [26] LHCb, M. Dorigo *et al.*, *FT workshop, intro and status*, LHCb-TALK,
 631 <https://indico.cern.ch/event/257864/session/0/contribution/37/material/slides/0.pdf>.
- 632 [27] LHCb, M. Dorigo *et al.*, *FT twiki page*, LHCb-TALK,
 633 <https://twiki.cern.ch/twiki/bin/viewauth/LHCbPhysics/FlavourTagging4Reco14>.
- 634 [28] R. Niet, *OS Calibration on $B^+ \rightarrow J/\psi(e^+e^-)K^+$ using EPM*,
 635 <https://indico.cern.ch/event/484452/>.
- 636 [29] LHCb, R. Aaij *et al.*, *Precision measurement of the $B_s^0 - \bar{B}_s^0$ oscillation frequency*
 637 *with the decay $B_s^0 \rightarrow D_s^+\pi^-$* , LHCb-ANA-2012-053.